AGU PUBLICATIONS

JGR

Journal of Geophysical Research: Oceans

RESEARCH ARTICLE

10.1002/2016JC011841

Seasonal and interannual variability of the Arctic sea ice: A comparison between AO-FVCOM and observations

Yu Zhang[1,2], Changsheng Chen[1,2], Robert C. Beardsley[3], Guoping Gao[1], Jianhua Qi[2], and Huichan Lin[2]

[1]Department of Marine Science and Technology, College of Marine Sciences, Shanghai Ocean University, Shanghai, China, [2]Department of Fisheries Oceanography, School for Marine Science and Technology, University of Massachusetts-Dartmouth, New Bedford, Massachusetts, USA, [3]Department of Physical Oceanography, Woods Hole Oceanographic Institution, Woods Hole, Massachusetts, USA

Key Points:
- The 37 year simulated sea ice was in good agreement with available observed sea ice extent, concentration, drift velocity, and thickness
- Intermodel comparisons show that the high-resolution AO-FVCOM provided better performance in the ice thickness simulation
- Sensitivity experiments were made to examine parameterizations of external and ice-water interfacial stresses on model-produced bias.

Correspondence to:
Y. Zhang,
yuzhang@shou.edu.cn

Citation:
Zhang, Y., C. Chen, R. C. Beardsley, G. Gao, J. Qi, and H. Lin (2016), Seasonal and interannual variability of the Arctic sea ice: A comparison between AO-FVCOM and observations, *J. Geophys. Res. Oceans*, *121*, doi:10.1002/2016JC011841.

Received 28 MAR 2016
Accepted 5 NOV 2016
Accepted article online 11 NOV 2016

Abstract A high-resolution (up to 2 km), unstructured-grid, fully ice-sea coupled Arctic Ocean Finite-Volume Community Ocean Model (AO-FVCOM) was used to simulate the sea ice in the Arctic over the period 1978–2014. The spatial-varying horizontal model resolution was designed to better resolve both topographic and baroclinic dynamics scales over the Arctic slope and narrow straits. The model-simulated sea ice was in good agreement with available observed sea ice extent, concentration, drift velocity and thickness, not only in seasonal and interannual variability but also in spatial distribution. Compared with six other Arctic Ocean models (ECCO2, GSFC, INMOM, ORCA, NAME, and UW), the AO-FVCOM-simulated ice thickness showed a higher mean correlation coefficient of ~0.63 and a smaller residual with observations. Model-produced ice drift speed and direction errors varied with wind speed: the speed and direction errors increased and decreased as the wind speed increased, respectively. Efforts were made to examine the influences of parameterizations of air-ice external and ice-water interfacial stresses on the model-produced bias. The ice drift direction was more sensitive to air-ice drag coefficients and turning angles than the ice drift speed. Increasing or decreasing either 10% in water-ice drag coefficient or 10° in water-ice turning angle did not show a significant influence on the ice drift velocity simulation results although the sea ice drift speed was more sensitive to these two parameters than the sea ice drift direction. Using the COARE 4.0-derived parameterization of air-water drag coefficient for wind stress did not significantly influence the ice drift velocity simulation.

1. Introduction

The Arctic Ocean is characterized by multiscale physical processes that are influenced significantly by the temporal and spatial variability of the sea ice (Figure 1). The sea ice produces a high albedo feedback in radiance balance and thus insulates or reduces the heat flux into and out of the ocean [*Hall*, 2004; *Perovich et al*., 2007; *Maykut and McPhee*, 1995; *Lytle and Ackley*, 1996; *Sturm et al*., 2002; *Screen and Simmonds*, 2010]. In a persistent ice coverage region, the near-surface water movement is driven predominately by the ice-sea interfacial stress in proportion to the shear of the ice-drifting and water velocities at the sea surface [*Hibler*, 1979; *Mellor et al*., 1986; *Proshutinsky and Johnson*, 1997; *Preller*, 1999; *Feltham et al*., 2002]. The sea ice is a key regional feature of the Arctic Ocean [*Serreze et al*., 2007] and an indicator of global climate change [*Flato and Boer*, 2001].

In the past three decades, the sea ice extent in the Arctic have dramatically decreased, with a linear regression trend of $\sim -4.00 \pm 0.18\%$/decade reported by *Comiso* [2012] based on data from November 1978 to 2010, and of $\sim -4.37 \pm 0.29\%$/decade updated with data covering the period of 1978–2014. The most significant reduction occurred in September, which showed a declining trend of $\sim 12.03 \pm 2.57\%$/decade. In particular, the sea ice extent dropped to $\sim 4.29 \times 10^6$ km^2 and $\sim 3.62 \times 10^6$ km^2 in September 2007 and 2012, respectively, accounting for a loss rate of ~32.57% and ~43.10% compared with the climatological mean value in September of 1979–2014. In the Arctic, the thinning of the sea ice thickness cooccurred with the declining of the sea ice extent [*Kwok and Rothrock*, 2009; *Rothrock et al*., 1999, 2008]. The measurements made on submarine cruises in the deep water of the Arctic basin showed that the mean sea ice thickness decreased from 3.1 m over the period 1958–1976 to 1.8 m over the period 1993–1997, accounting for a loss rate of 41.9% [*Rothrock et al*., 1999], and from a peak of 3.42 m in 1980 to a minimum of 2.29 m in 2000,

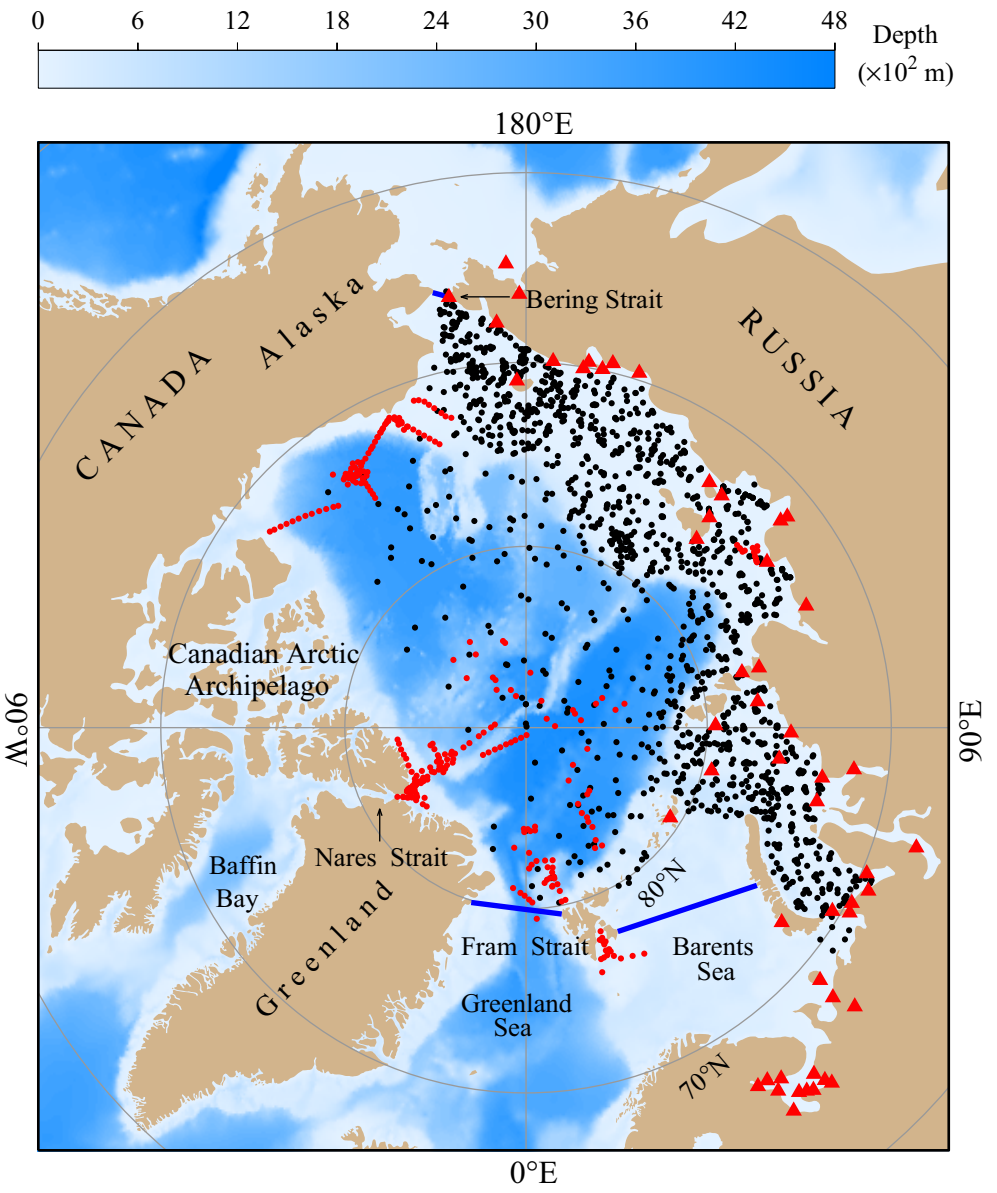

Figure 1. Bathymetry of the Arctic Ocean and the locations where the sea ice thickness measurements were made. Four types of sea ice thickness data were used for model-data comparisons, including the Ice, Cloud, and land Elevation Satellite (ICESat) campaigns, the electromagnetic airborne (EM-Airborne) measurements (red dots), Romanov atlas (Romanov-Atlas) data (black dots), and 51 coastal fast ice stations (Coastal-Stations) data (red triangles). Blue lines indicate the sections where the sea ice drift fluxes were estimated.

accounting for a loss rate of 33.0% [*Rothrock et al.*, 2008]. The satellite data in the deep water over the period 2003–2008 showed that the mean declining rates in the winter and summer are −0.10 and −0.20 m/yr [*Kwok and Rothrock*, 2009]. The faster ice melting was believed due to climate warming, which was evident in the air temperature record north of 60°N which showed a warming rate of 0.72 ± 0.10°C per decade over the period 1981–2005 [*Comiso*, 2006].

In order to understand the sea ice dynamics and its roles in climate change, a variety of ice-sea coupled numerical models had been developed with an aim at reproducing the temporal and spatial variability of the sea ice in the Arctic Ocean [e.g., *Hibler*, 1979; *Zhang and Rothrock*, 2003; *Hunke et al.*, 2010; *Terwisscha van Scheltinga et al.*, 2010; *Gao et al.*, 2011; *Mårtensson et al.*, 2012]. *Zhang and Rothrock* [2003] applied a 4/5°-resolution global Parallel Ocean and Ice Model (POIM) to the sea ice in the Arctic Ocean, and compared with observed ice-drifting velocity, concentration, extent, and thickness for the year 1993. The POIM was

robust to capture properties of sea ice observations with an uncertainty range of ~10%. Similar efforts were made for the period 1979–2007 by *Terwisscha van Scheltinga et al*. [2010] with a high-resolution (from a few hundred meters in narrow straits to ~200 km in the open basin) Finite-Element coupled Sea-ice-Ocean Model (FESOM) and for the period 1980–2002 by *Mårtensson et al*. [2012] using a 0.25°-resolution Rossby Centre Ocean model (RCO). The FESOM was capable of reproducing the anomaly of the sea ice area, although the extent was overestimated by ~20% in winter. With adequate geometric resolution in narrow straits, this model suggested that the variability of the sea-ice volume flux through most straits was highly correlated with the Arctic Oscillation (AO), increasing and decreasing during positive and negative AO phases. The RCO captured the decreasing trend of the ice extent anomaly in September observed over the period 1980–2002, but with a ~40% underestimation. This model also reasonably simulated the ice thickness and drifting velocity, although in some regions the model-data difference was up to 67% for the ice thickness and ±20 cm/s for the ice drifting velocity, respectively. It should be noted that in the Arctic Ocean, the observed ice drifting velocity was generally in an order of ~2–3 cm/s with a maximum value of ~30 cm/s.

Johnson et al. [2007, 2012] made intermodel comparisons for the ice concentration and thickness, respectively. The first was made for the period 1979–1999 among nine models from Alfred Wegener Institute (AWI1, AWI2), Goddard Space Flight Center (GSFC), Institute for Computational Mathematics and Mathematical Geophysics (ICM), Institute of Ocean Sciences (IOS), the Los Alamos National Lab (LANL), Naval Postgraduate School (NPS), Russian Academy of Science (RAS), and the University of Washington (UW). The second was made among six models: ECCO2-Estimating the Circulation and Climate of the Ocean, Phase II from Jet Propulsion Laboratory; the GSFC model (hereafter referred to as GSFC); INMOM-Institute of Numerical Mathematics Ocean Model; ORCA-the National Oceanography Centre Southampton model; NAME-the Naval Postgraduate School Arctic Modeling Effort; and the UW model (hereafter referred to as UW)-Pan-Arctic Ice-Ocean Modeling and Assimilation System of the University of Washington. For ice concentration, nine models showed similar performance in the winter but were significantly diverse in the summer and fall. For September, for example, AWI1, AWI2, UW, NPS, IOS, ICM, LANL, and GSFC models underestimated the ice concentration up to 40% in the central Arctic Ocean, while it was overestimated by ~10% with RAS. The model-data difference was caused not only by model performance but also by the uncertainty of satellite measurements due to melt ponding and surface wetness. Similarly diverse results were also found in the ice thickness, with the model-data difference for six models in the range from 8.4% to 32.8%.

The diverse performance of these models was believed due to the differences in grid resolution, bathymetry and coastline approximation, sea ice dynamics and thermodynamics, discrete algorithm, external driving forcing, and lateral boundary conditions [*Johnson et al*., 2012]. It is clear that we still remain in a state with an insufficient validation of sea ice models, especially on the long-term variability and detailed spatial distribution. Availability of the long-term sea ice data in the past decades provides us such an opportunity to conduct a more comprehensive model-data comparison experiment with inclusion of all types of sea ice properties such as sea ice extent, concentration, thickness, and drift velocity. A high-resolution, fully coupled sea ice-ocean, Arctic-global nested model was developed based on the three-dimensional unstructured-grid, Finite-Volume Community Ocean Model (hereafter referred to as AO-FVCOM) [*Chen et al*., 2003, 2006, 2009, 2013, 2016; *Gao et al*., 2011]. The sea ice model implemented in the AO-FVCOM is UG-CICE-the Unstructured Grid version of the Los Alamos Community Ice Code (CICE) developed by *Gao et al*. [2011]. The CICE, developed by *Hunke et al*. [2010], is governed by energy-conserving thermodynamics equations with five ice thickness categories (four layers of ice and one layer of snow), Elastic-Viscous-Plastic (EVP) ice momentum equations [*Hunke and Dukowicz*, 1997; *Hunke*, 2001], and energy-based ridging schemes of *Thorndike et al*. [1975], *Hibler* [1979], and *Lipscomb et al*. [2007] as well as ice strength parameterizations given by *Rothrock* [1975]. Converting CICE to UG-CICE on the FVCOM framework improves its flexibility in resolving the complex coastal geometry and steep continental slopes. The UG-CICE was validated for benchmark- idealized problems and through comparison with the observed climatologically averaged sea ice extent and drift velocity in the Arctic Ocean [*Gao et al*. 2011]. Built on this success, we have applied AO-FVCOM to simulate the sea ice and circulation in the Arctic Ocean over the period 1978–2014. This long-term simulation allows us to evaluate the AO-FVCOM performance for its ability to capture the interannual variability of the sea ice in the Arctic Ocean.

The rest of the paper is organized as follows. In section 2, the AO-FVCOM is briefly described, following the design of numerical experiments and list of observational data used for the model-data comparison. In section 3, the AO-FVCOM-simulated sea ice results are presented and discussed though comparison with observed sea ice extent, concentration, drift velocity, and thickness. In section 4, a further intermodel comparison is made for the sea ice thickness between the AO-FVCOM and other six numerical models (included in *Johnson et al*. [2012]). In section 5, sensitivity experiments are made to examine the simulated ice drift velocity bias due to different parameterization of air-ice external and ice-water interfacial stresses. In section 6, the conclusion summarizes the major findings.

2. AO-FVCOM, Data, and Design of Numerical Experiments

2.1. AO-FVCOM

The AO-FVCOM is an integrated Arctic-global ice-sea coupled ocean model system configured with the version 3.1 source code of FVCOM [*Chen et al*., 2016]. The FVCOM is a prognostic, unstructured-grid, Finite-Volume, free-surface, 3-D primitive equation Community Ocean Model [*Chen et al*., 2003, 2006, 2013]. The UG-CICE is a sea ice module in FVCOM, which is implemented into the AO-FVCOM by coupling the ice mass, ice stress, and heat exchange at the ice-sea interface [*Gao et al*., 2011]. The governing and finite-volume discrete equations of UG-CICE and coupling with AO-FVCOM were described in detail by *Gao et al*. [2011] and *Chen et al*. [2016].

The AO-FVCOM was configured with a nonoverlapped triangular grid with a horizontal resolution varying from 2 to 40 km (Figure 2). The grid was designed to better resolve topographic and baroclinic dynamical scales over the Arctic slope and narrow straits in the CAA [*Chen et al*., 2016], and the triangles were created

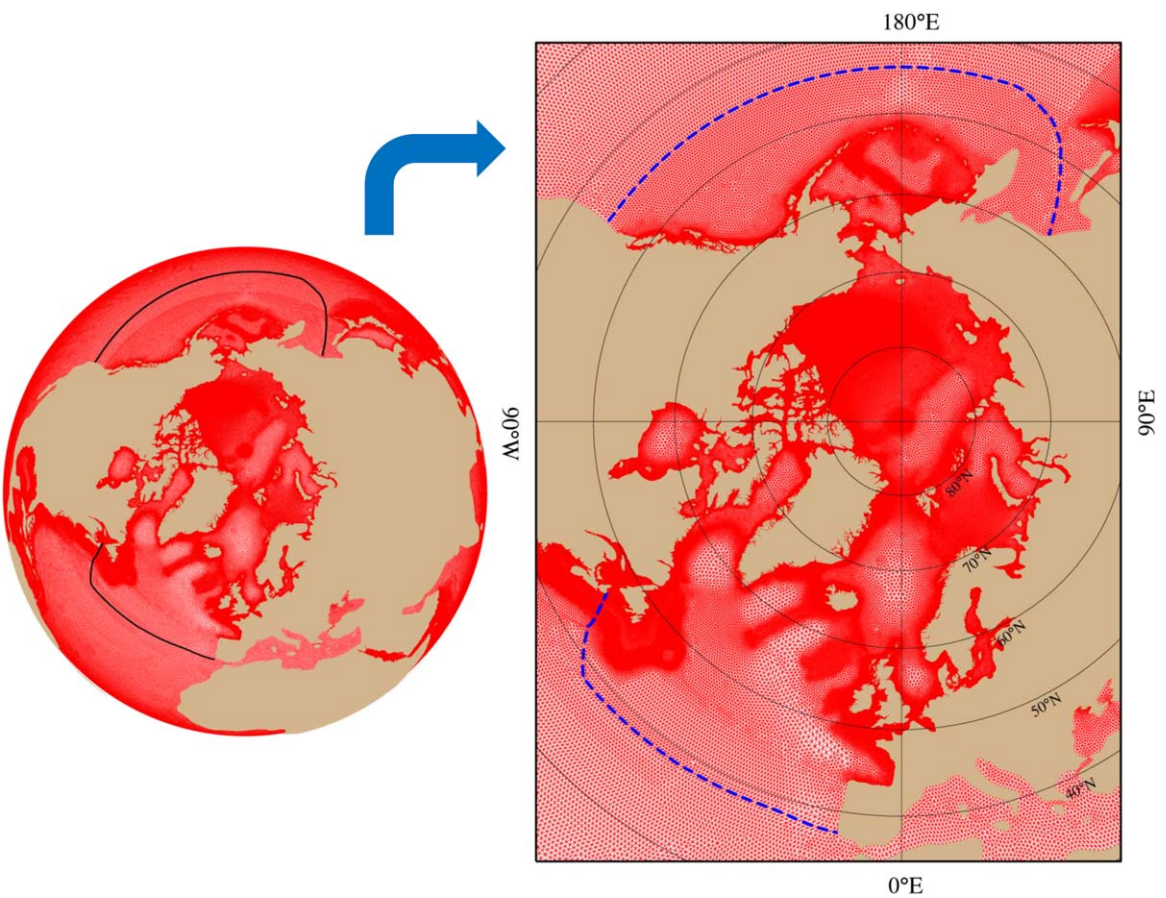

Figure 2. The illustrations of the unstructured triangular grids of the AO-FVCOM/Global-FVCOM with the horizontal resolution varying from 2 to 5 km in the Canadian Arctic Archipelago and 10–40 km in the interior basins. Blue-dashed lines indicate the boundary cells nesting to Global-FVCOM.

by following the criteria to make sure the areas of adjacent meshes satisfied a ratio that could avoid the discontinuity and stability in numerical performance.

The domain covered the entire Arctic Ocean and the adjacent Pacific and North Atlantic Oceans, including the CAA, the Labrador, Greenland, and Norwegian Seas, Hudson and Baffin Bays. It was bounded by two open boundaries nesting to the Global-FVCOM: one in the Atlantic Ocean at the north of $\sim$39° and the other in the Pacific Ocean at the north of $\sim$45°. A hybrid terrain-following coordinate with a total of 45 layers was used in the vertical. In the regions where the water depth was $>$ 225 m, the s-coordinate is used, in which 10 and 5 uniform layers (thickness of 5 m) were specified near the surface and bottom, respectively. In the shallow continental and coastal regions where the water depth was $<$ 225 m, the σ-coordinate with the same total number of vertical layers was used. These two coordinates have a transition at the 225 m isobaths at which the thickness of all layers was 5 m. A detailed description was given in *Chen et al*. [2013] and *Zhang et al*. [2016].

The AO-FVCOM was initialized with the 50 year spin-up output under a "climatologic" meteorological forcing and river discharge conditions [*Gao et al*., 2011] and driven by (a) astronomical tidal forcing with eight constituents (M_2, S_2, N_2, K_2, K_1, P_1, O_1, and Q_1), (b) surface forcing (surface wind stress, net heat flux plus shortwave irradiance in the water column, air pressure gradients, and precipitation minus evaporation), and (c) river discharges. The surface forcing was taken from the 6 hourly version-2 data set for Common Ocean-ice Reference Experiments (CORE-v2) over the period 1978–2009 [*Large and Yeager*, 2009] and then the National Center for Environmental Prediction and the National Center for Atmospheric Research (NCEP/NCAR) data set over the period 2010–2014 [*Kalnay et al*., 1996]. The detailed explanation was given in *Zhang et al*. [2016]. A total of 225 rivers were included. The river discharges collected from the U.S. Geological Survey and the Water Survey of Canada were specified using daily real-time records. Ten major Russian rivers (Indigirka, Khatanga, Kolyma, Lena, Ob, Pechora, Pur-Taz, Severnaya Dvina, Yana, and Yenisei River) were included with the monthly discharge data provided by A. Proshutinsky (personal communication, 2015). For the rivers without real-time discharge records, the climatological records were used from the Navy global river data sets.

The AO-FVCOM simulation was conducted through one-way nesting with Global-FVCOM. The Global-FVCOM has been run for the period 1978–2014 with the data assimilation of satellite-derived global daily sea surface temperature (SST), sea surface height (SSH), and monthly T/S observational data (e.g., NODC, JAMSTEC, Argo) in the south of 62.5°N. The assimilation used in the Global-FVCOM was aimed at providing the best knowledge boundary condition for the AO-FVCOM. The AO-FVCOM simulation began on 1 January 1978, with the initial condition of temperature and salinity provided by the Global-FVCOM, and was integrated over the 37 years until 31 December 2014. Since AO-FVCOM used the same time step of 300 s as Global-FVCOM and the nesting boundary of the AO-FVCOM shared the same grid nodes and cells with Global-FVCOM, the boundary condition of the AO-FVCOM was directly specified by the output of Global-FVCOM at each time step through the one-way nesting. For the sea ice assimilation, no data assimilation was carried out for either hydrodynamics or sea ice in the AO-FVCOM.

2.2. Observational Data

The AO-FVCOM-simulated sea ice was compared with multiple types of ice observational data including sea ice extent, concentration, drift velocity, and thickness. The ice extent data were from the National Snow and Ice Data Center (NSIDC) [*Fetterer et al*., 2002]. The data set covered our simulation period over 1978–2014. Since the NSIDC data only contained monthly values, we used Bootstrap sea ice concentration data, which included both daily and monthly spatial distributions, to recalculate the monthly values of ice extent and defined the difference between NSIDC and Bootstrap-derived values as an uncertainty due to discrete algorithms used to estimate the ice extent.

The sea ice concentration data used in this study were the 25 km resolution monthly ice concentration data which were derived from the satellite measurements with the Advanced Microwave Scanning Radiometer-Earth Observing System (AMSR-E) Bootstrap Algorithm [*Comiso*, 2000].

The ice drift velocity data were from the NSIDC, which was derived from the combined passive microwave radiometer measurements and buoy data (the International Arctic Buoy Program) [*Tschudi et al*., 2016]. The

data were available over the period November 1978 through December 2014, with a spatial coverage from 48.4°N to 90°N and a horizontal resolution of 25 km.

The ice thickness data were from four sources (Figure 1), which was compiled and provided by A. Proshutinsky (personal communication, 2015). The first was from the Ice, Cloud, and land Elevation Satellite (ICESat) campaigns over the period 2003–2008, with a total of five fall and five winter measurements through the Geoscience Laser Altimeter System covering the entire central Arctic Ocean [*Kwok et al.*, 2009]. The five fall campaigns were taken during the September–November period and the five winter campaigns were during the February–April period. Each of these campaigns was done with operational days varying from 34 to 55 days. This data set has a horizontal resolution of 25 km. The second was from the electromagnetic airborne measurements (hereafter referred to as "EM-Airborne"), which were carried out mainly in the Arctic Basin and near Nares Strait and Fram Strait (Figure 1: red dots) [*Haas et al.*, 2009]. The data covered the period 2001–2009 excluding 2002, during which the survey was taken over two periods of March or April or May and August or September, respectively. The third was from the Atlas of Ice and Snow of the Arctic Basin and Siberian Shelf Seas (Figure 1: black dots) (hereafter referred to as "Romanov-Atlas"). This data set covered the period of 1930s–1989 [*Romanov*, 1995], with the 1978–1989 campaigns focusing on the spring time (March–May). The fourth data set was the drill-hole, fast sea ice thickness measurements at 51 coastal stations over the Russian coast and islands which were from the Arctic and Antarctic Research Institute, Russia (Figure 1: red triangles) (hereafter referred to as "Coastal-Stations"). The data covered the period 1998–2008. It should be noted that the second and fourth data sets had relatively sparse coverage with a relatively larger uncertainty.

2.3. Design of Numerical Experiments

The numerical experiments were first made by a real-time simulation over the period 1978–2014 and the results were validated through comparisons with observations. Then, a series of process-oriented experiments were carried out to examine the sensitivities of the simulated sea ice to parameterizations of the air-ice external and ice-water interfacial stresses, with an objective of understanding the dynamic causes for the model-data difference due to model performance and parameterization.

3. Comparisons With Observations

3.1. Sea Ice Extent

The AO-FVCOM reproduced the observed sea ice extent over the simulation period 1978–2014, not only for the monthly mean but also for the anomaly (Figure 3). The correlation between simulated and observed ice extents was 0.99 with a critical value of 0.09 at a 95% significance level. The difference between model-simulated and observed sea ice extents was in the range of $5.60 \times 10^2 - 1.88 \times 10^6$ km^2, with a mean absolute difference and root mean square (RMS) errors of 0.42×10^6 km^2 and 0.54×10^6 km^2, respectively. In the months when minimum and maximum differences were found, the model-data difference only accounted for ~0.01% and ~17.67% of the total sea ice coverage area, respectively. Similarly, the simulated and observed anomalies of sea ice extent were highly correlated. Given the critical value of 0.09 at a 95% significance level, the correlation coefficient was 0.88. The linear least-square regression of the observed sea ice anomaly showed a decreasing trend at -5.25×10^4 km^2/yr over the last 37 years, this trend was reasonably captured by AO-FVCOM, especially after year 2000. The model-simulated mean decreasing trend was -3.76×10^4 km^2/yr, which was lower than the observed decreasing trend. This difference was mainly caused by the model-data discrepancy in the summertime sea ice extent, which was underestimated over the period 1980–1998 and overestimated over the period 2008–2011. The largest underestimated difference was 0.92×10^6 km^2, occurring in September 1981 and the largest overestimated difference was 0.63×10^6 km^2, occurring in September 2008. They accounted for the differences of 12.7% and 13.3% relative to the observed values, respectively.

This difference was believed due mainly to the model performance with imperfect dynamics setup and parameterizations used in the ice-current coupled model, which were associated with (1) the average methods to calculate the monthly mean value, (2) grid resolutions, and (3) downward longwave radiations. There were two sources of NSIDC ice extent data: (1) monthly averaged data and (2) daily data. The AO-FVCOM-simulated ice extents were output at a daily time scale and averaged monthly. To be consistent with the method used in the AO-FVCOM, the daily Bootstrap ice concentration was interpolated onto the AO-

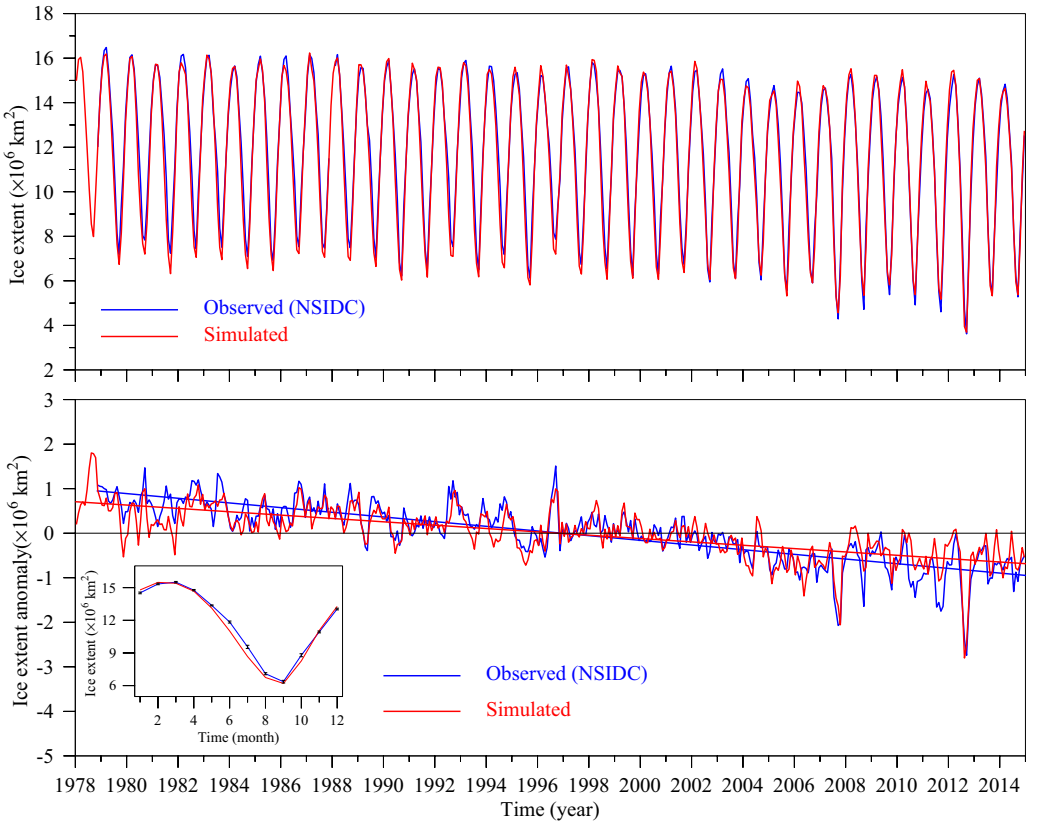

Figure 3. Comparison of simulated (red) and observed (blue) (top) monthly sea ice extents and (bottom) anomalies over the period 1978–2014. The straight lines are the linear regression trends estimated by AO-FVCOM (red) and NSIDC (blue) anomalies. The figure inserted in the bottom plot shows the model-simulated and observed seasonal variability of the ice extent averaged over the period 1978–2014. The black vertical bar in that figure is the standard deviation derived using the NSIDC data and the Bootstrap-derived data.

FVCOM grid nodes and the monthly mean sea ice extent was averaged with the same approach as the model. Comparing with the NSIDC-provided monthly ice extent, the mean absolute difference and RMS uncertainty over the period 1978–2014 was 0.17 $\times$ 10^6 km^2 and 0.22 $\times$ 10^6 km^2, respectively. These differences accounted for 40.5% and 40.7% of the data-model mean absolute differences and RMS errors reported in the original comparison. Also, since the spatial and time coverage of the satellite-derived NSIDC data varies day to day, the model-data comparisons were not always based on the same sampling numbers. Therefore, about 10% of the model-data discrepancy should be reasonable.

The AO-FVCOM-computed monthly sea ice extent was estimated based on the areas of individual triangle grid cells covered by the sea ice, with accuracy depending on grid resolution. The monthly Bootstrap-derived sea ice coverage area was interpolated onto the model grid nodes and the observed sea ice extent was recalculated based on the same grid resolution as the model. The mean absolute difference and RMS error between the NSIDC-provided and recalculated sea ice extents over the period 1978–2014 was 0.21 $\times$ 10^6 km^2 and 0.26 $\times$ 10^6 km^2. The bias caused by grid resolution accounted for 50.0% and 48.1% for the mean absolute difference and RMS error regarding the model-data discrepancy found in the original comparison. This bias also varied seasonally, relatively large during the rapid ice melting period of June–August, during which the model overestimated the ice melting (Figure 3, bottom plot).

The experiments were also made to examine how the model-simulated ice extent was sensitive to the parameterization used in the heat flux estimation. In the CICE, there are two empirical formulations for the downward longwave radiation. One is derived by *Parkinson and Washington* [1979] (hereafter referred to as the PW-formulation) and the other is derived by *Rosati and Miyakoda* [1988] (hereafter referred to as the RM-formulation). The PW-formulation is given as

$$F_{lw\downarrow} = \epsilon\sigma T_a^4\left[1-0.261\exp\left(-7.77\times10^{-4}T_a^2\right)\right](1+0.275f_{cld}) \quad (1)$$

where $F_{lw\downarrow}$ is downward longwave radiation; ϵ is the emissivity of the ocean (0.97); σ is the Stephan-Boltzman constant; T_a is the surface air temperature (K); and f_{cld} is the cloud cover fraction. The RM-formulation is defined as

$$F_{lw\downarrow} = \epsilon\sigma T_s^4 - \epsilon\sigma T_a^4\left(0.39-0.05e_a^{1/2}\right)(1-0.8f_{cld}) - 4\ \epsilon\sigma T_a^3(T_s-T_a) \quad (2)$$

where T_s and T_a are the ocean and air surface temperature; e_a is the atmospheric vapor pressure (mb).

Gao et al. [2011] tested these two formulations in their simulation experiment of the sea ice in the Arctic Ocean under the climatological mean condition. They found that the simulated sea ice extent is sensitive to the formulations used to estimate downward longwave radiation, and the PW-formulation could significantly produce larger ice melting. For this reason, they selected the RM-formulation in the AO-FVCOM. In this study, we followed their recommendation and retained the RM-formulation for the ice simulation over the period 1978–2014. The model-data discrepancies reported in our comparison could be also due to the downward longwave radiation. The AO-FVCOM was rerun over the time period of September 1981 using the PW-formulation. The comparison between the ice extents obtained from the model run with the RW-formulation and the PW-formulation showed that the ice extent dropped by an amount of 0.08×10^6 km^2, which could increase the model-data difference by 8.70%. The same types of experiments were also made over the period of September 2008, which also showed a drop by an amount of 0.12×10^6 km^2, which decreased the model-data difference by 19.05%. It seemed like the performance of these two formulations differed over the different period under different environmental conditions. Although we could not determine which one is better, the comparison results at least showed that the simulated ice extent was sensitive to the empirical formulation used to estimate the downward longwave radiation. The fact that the differences estimated in the yearly results with the PW-formulation and the RW-formulation were in the same range of the model-data discrepancy reported in our comparison implied that the error could be related to the parameterization used in the downward longwave radiation.

If the reasons discussed above were taken into account, we could reasonably conclude here that AO-FVCOM was capable of reproducing the observed seasonal and interannual variability of the sea ice extent in the Arctic Ocean.

3.2. Sea Ice Concentration

We compared the simulated and observed sea ice concentrations over the period 1979–2014. Examples are shown in the top plots of Figure 4 for 36 year seasonal means: spring (March–May), summer (June–August), fall (September–November), and winter (December–February) and in the bottom plot of Figure 4 for the monthly anomaly. The distributions of the observed sea ice concentration in spring and winter were very similar: most of the Arctic area was fully covered by the high concentration sea ice of $>$0.9, with ice-free boundaries in the southern region of Baffin Bay and off the eastern slope of Greenland and southern shelf of the Barents Sea connecting to the North Atlantic Ocean. This distribution pattern was reasonably captured by AO-FVCOM, except that the simulated ice coverage area was relatively wider over the eastern shelf of Greenland, extended more south out of the southern shelf of the Barents Sea and in the Baffin Bay. During summer and fall, the sea ice coverage area shrank toward the Arctic, with significant decreases of the ice concentration in the Bering Sea, CAA, and Baffin Bay, over the eastern shelf of the Greenland and the southern shelf of the Barents Sea and along the coastal area of Alaska and Russia. These changes were also reasonably captured by AO-FVCOM, even though the model overestimated the sea ice cover in the marginal ice zone in the Greenland and Barents Seas. During summer, the simulated ice concentration was $\sim$10% and $\sim$5% higher near the Russian coast and in Baffin Bay, respectively, while $\sim$5% lower in the central Arctic. During fall, the major difference between simulated and observed sea ice concentrations was mainly in the central Arctic, which accounted for $\sim$5% of the total ice concentration. We did not expect that the model could exactly reproduce the observed sea ice concentration since the thermal dynamics implemented in CICE and also UG-CICE depend highly on the empirical formulation with prespecified parameterizations in heat flux estimation. The shortwave radiation, sensible and latent heat fluxes, incoming and outgoing longwave radiations were obtained from the global CORE-v2 and NCEP atmospheric model. Since no direct measurements were available to evaluate the accuracy of CORE-v2-predicted and NCEP-predicted

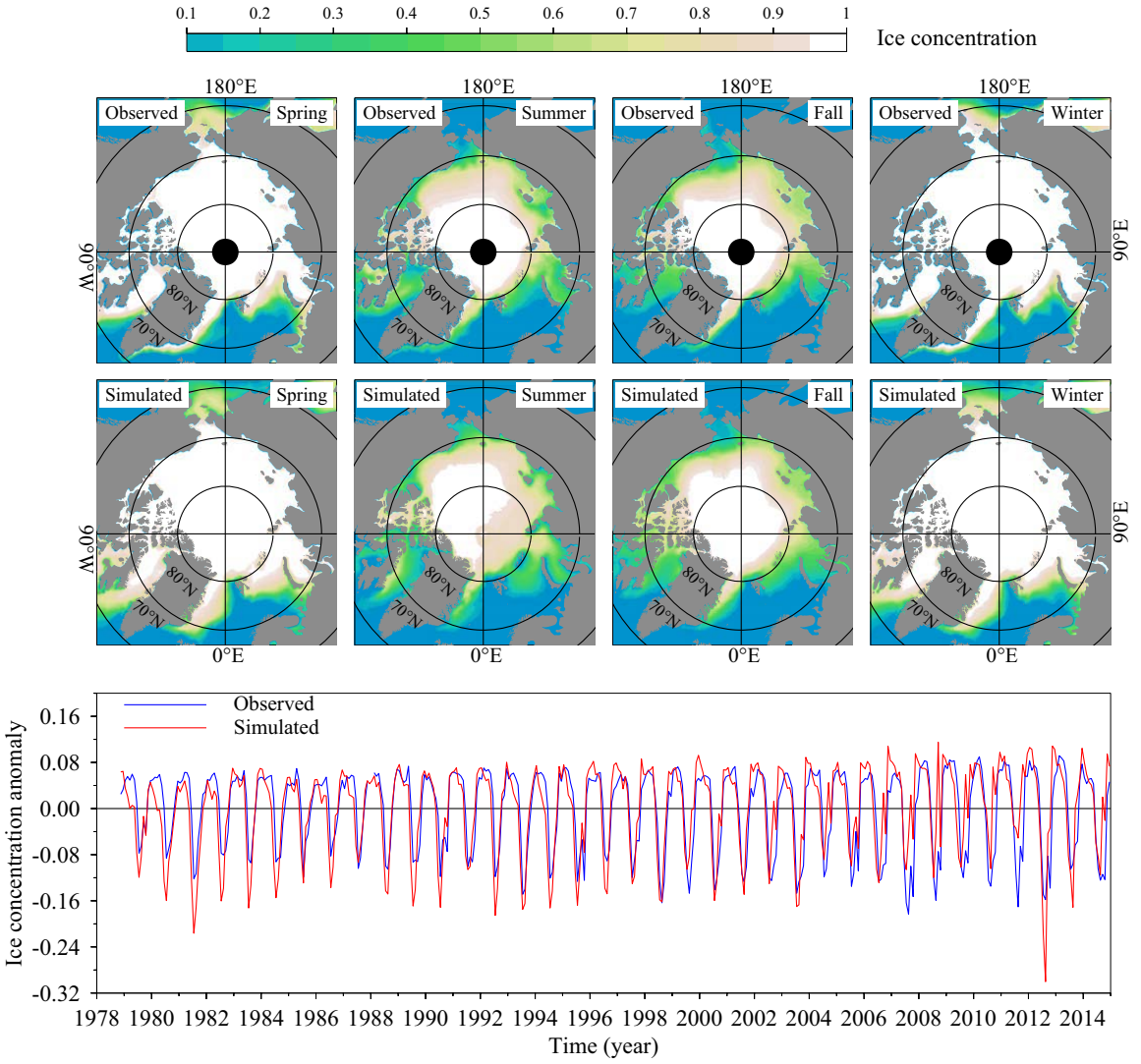

Figure 4. (top) Comparison of the model-simulated and observed seasonal mean sea ice concentrations for spring, summer, fall, and winter over the period 1979–2014. The observed ice concentrations were from the Bootstrap data. The black circle in figures for observations is the area where the satellite measurements were not available. (bottom) Comparison of simulated and observed anomalies of monthly sea ice concentration averaged over the entire Arctic Ocean north of 50°N for the period 1978–2014.

heat flux in the Arctic Ocean, the large model-data discrepancy in the local region could be related to the error of the predicted heat flux and the spatial variation of CORE-v2-predicted and NCEP-predicted heat flux. In addition, since the ice-ocean heat flux was estimated by parameterized empirical formulations, and different formulations could have significantly different performance in the different time and locations, the large error of the sea ice concentration could be also related to parameterization methods used in the model. The experiments with the PW-formulation and the RW-formulation for the download longwave radiation suggested that the difference of sea ice extent produced by the two formulations could have the same error range with the model-data discrepancy reported in the original comparison. The same error range was also reported in the sea ice concentration. In the experiments, it was found that the surface water temperature also played a significant role in the sea ice melting and growth. The inaccuracy produced in the model-computed surface water temperature varied in space and time, which could directly contribute to the error in the sea ice concentration. Since multiple reasons were related to the model error in the sea ice concentration and the AO-FVCOM experiments were made with the model-produced external forcing with an unknown uncertainty, it was difficult to dig out the relative contributions from these factors.

We also compared the simulated and observed anomalies of monthly mean sea ice concentration in the Arctic Ocean over the period 1978–2014 (Figure 4, bottom plot). The mean sea ice concentration in the

Arctic Ocean was defined as the ratio of sea ice area to sea ice extent. Sea ice area was the total area covered by the sea ice within the data cells with a threshold at 15% sea ice concentration. In the region around the North Pole, the ice concentration data were not captured by satellite sensors, we just simply assumed the concentration was 1.0 there. The observed and simulated 37 year mean ice concentrations were 0.82 and 0.88, with standard deviations of 0.07 and 0.08, respectively. Although the model overestimated the mean sea ice concentration by a factor of ~7.3% over the 37 year period, the model produced a variation range of the sea ice concentration similar to the observations. The model-simulated and observed anomalies were in the same phase with a correlation coefficient of 0.80, which was significantly higher than a critical value of 0.09 at a 95% significance level. The mean absolute difference and RMS error between observed and simulated anomalies of the sea ice concentration were 0.03 and 0.05, respectively. Considering an observed maximum anomaly of ~0.18, the mean difference accounted for ~16.7% of the observed anomaly peak value.

The simulated ice concentration anomalies showed larger negative values than the observed anomalies with a mean difference of 0.04 in the summer over the periods 1979–1996 and 2012–2013 and showed smaller negative values than the observed anomalies with a mean difference of 0.08 in the summer over the period 2004–2011. It was mainly caused by the errors of the simulated sea ice area since the summer sea ice area was underestimated over the periods 1979–1996 and 2012–2013 and overestimated over the period 2004–2011. Since the mean sea ice concentration in the Arctic region was defined as the ratio of the sea ice area to the sea ice extent, the inaccurate estimation in either the sea ice area or the sea ice extent could cause the error in the sea ice concentration. Similar to the sea ice extent, the estimated uncertainty of the sea ice area was also related to the impact of varying grid resolutions, the method used to average the monthly mean value and downward longwave radiation.

It should be pointed out here that the UG-CICE was the unstructured grid version of CICE, which retains the same formulation except being solved over the unstructured grid finite-volume platform of FVCOM. In the CICE, the sea ice is assumed to be a mixture of individual constituents with different thickness. Five ice categories, which included one layer of snow and four layers of ice (0–0.6 m, 0.6–1.4 m, 1.4–2.4 m, and 2.4–3.6 m), were set. For the open-water ice growth, the ice growth is caused by the potential heat from the ocean when the surface water temperature is lower than the freezing temperature. The ice melting and growth consist of surface, bottom, and lateral changes. Surface melting and growth are controlled by the difference between the net heat flux from the atmosphere to the ocean and the conductive flux from the top surface to the ice interior. Bottom melting and growth are controlled by the difference between the conductive heat flux at the bottom surface and the net heat flux between ice and ocean. Lateral melting and growth are controlled by the interfacial heat exchange between the ocean and side boundaries of the ice. In the real environment of ice growth, the variation process of sea ice from grease ice to nilas ice to young ice is considered but this process was not taken into account in CICE or UG-CICE [*Gao et al*., 2011].

3.3. Sea Ice Drift Velocity

We compared the daily-averaged observed and model-simulated ice drift velocity in the Arctic where the data were available over the period 1979–2014, and statistics are given in Table 1 for yearly mean speed and direction. Both the model-simulated and observed sea ice drift velocities had minimum values in 1984 and maximum values in 2007. Although the ice drift velocity varied significantly in space and with time, the mean drift velocity averaged over the entire basin was in the order of a few centimeters per second. The mean absolute value of the difference between model-simulated and observed spatially averaged ice drift velocities over a 36 year period was 0.7 cm/s, with a RMS value of 1.6 cm/s. Considering a 36 year-averaged observed mean ice drift velocity of 2.0 cm/s, the mean difference accounted for an error of 25.0%. If we estimate this mean difference relative to a 36 year-averaged observed maximum ice drift velocity of 12.8 cm/s, it accounted for an error of 3.9%. The differences between model-simulated and observed sea ice drift velocity directions were relatively larger than the speeds. The mean absolute value of the direction difference over a 36 year period was 30.1°, with a RMS value of 44.8°.

The AO-FVCOM reasonably captured the spatial distribution and temporal (monthly to seasonal-interannual) variability of the ice drift velocity in the Arctic Ocean. Examples are shown in Figure 5 for the comparison of the spatial distribution of seasonally averaged model-simulated and observed sea ice drift velocities. We first interpolated the model-simulated sea ice drift velocity onto the locations where the observational data

Table 1. Comparison of the Yearly Mean Sea Ice Velocity Between AO-FVCOM and Observation During the Period 1979–2014[a]

Year	Number of Samples	$\bar{V}_{obs}$ (cm/s)	$\bar{V}_{model}$ (cm/s)	$\lvert\Delta V\rvert$ (cm/s)	ΔV RMS (cm/s)	$\lvert\Delta\alpha\rvert$ (°)	$\Delta\alpha$ RMS (°)	V_{obs} Max (cm/s)	V_{model} Max (cm/s)
1979	14,155	1.3	2.3	1.0	2.2	30.4	44.0	8.1	21.8
1980	13,632	1.2	2.3	1.1	2.0	31.2	46.3	10.5	16.2
1981	13,889	1.3	2.6	1.3	2.4	27.6	41.6	7.5	22.3
1982	13,957	1.7	2.8	1.1	2.2	23.0	35.0	10.0	21.7
1983	13,293	1.4	2.3	1.0	2.1	32.0	45.2	10.2	23.0
1984	13,118	0.9	1.7	0.8	1.8	35.2	49.9	8.8	19.2
1985	13,594	1.5	2.3	0.8	1.5	25.4	39.6	10.6	14.2
1986	13,848	1.3	1.9	0.7	1.6	38.3	55.4	9.1	16.4
1987	13,940	1.7	2.4	0.8	1.5	24.1	38.5	9.8	15.6
1988	14,125	1.9	2.5	0.7	1.4	22.9	35.0	12.5	17.3
1989	14,002	1.6	2.4	0.8	1.9	30.9	45.0	9.6	20.8
1990	13,768	1.4	2.3	1.0	2.0	42.3	56.3	8.4	20.1
1991	13,597	1.5	2.2	0.7	1.6	27.7	42.3	8.5	18.3
1992	13,573	1.7	2.2	0.6	1.4	34.5	50.8	10.0	18.7
1993	13,591	1.8	2.4	0.6	1.5	41.4	57.9	19.2	20.3
1994	13,653	1.9	2.6	0.8	1.7	29.5	44.5	13.0	23.5
1995	13,505	2.3	3.3	1.1	2.2	21.4	34.3	14.8	23.3
1996	13,873	1.4	2.0	0.6	1.4	40.0	57.3	9.9	14.6
1997	14,186	1.9	2.5	0.7	1.4	27.1	43.0	9.9	16.2
1998	14,108	2.1	2.7	0.8	1.6	27.8	42.4	14.2	20.4
1999	13,676	1.9	2.7	0.9	1.6	22.7	33.5	15.6	20.1
2000	13,404	2.0	2.8	0.9	1.9	28.7	41.8	13.8	19.9
2001	13,704	2.0	2.5	0.7	1.4	30.0	45.0	15.7	14.5
2002	13,593	1.9	2.4	0.5	1.1	30.3	43.8	15.6	14.4
2003	13,798	2.5	2.7	0.6	1.3	37.5	54.2	16.0	15.7
2004	13,681	2.7	3.1	0.7	1.9	26.5	41.0	15.8	22.1
2005	13,405	2.3	2.9	0.8	1.8	28.3	42.9	14.5	19.3
2006	13,115	2.1	2.5	0.6	1.5	30.2	45.8	18.4	19.3
2007	13,153	3.4	3.9	0.8	1.7	22.0	36.2	14.2	19.7
2008	13,191	3.1	3.3	0.7	1.5	28.0	43.0	15.6	18.9
2009	13,363	2.5	2.8	0.6	1.5	30.2	43.9	16.8	20.4
2010	13,426	2.9	2.7	0.4	0.9	26.4	41.9	19.8	16.0
2011	13,313	2.4	2.6	0.4	1.1	30.3	44.4	12.5	15.1
2012	13,024	1.9	2.0	0.4	0.8	45.5	63.5	16.8	13.6
2013	13,343	2.5	2.5	0.4	0.8	29.9	46.7	14.4	13.2
2014	13,302	2.6	2.6	0.4	0.9	25.7	39.0	9.0	12.9
Mean	13,608	2.0	2.5	0.7	1.6	30.1	44.7	12.8	18.3

[a]Note: $\bar{V}_{obs}$ and $\bar{V}_{model}$ are the observed and simulated mean velocities. $\lvert\Delta V\rvert$ and ΔV RMS represent the mean absolute differences and root mean square differences of sea ice drift speed between the observation and model. $\lvert\Delta\alpha\rvert$ and $\Delta\alpha$ RMS represent the mean absolute differences and root mean square differences of sea ice drift direction, respectively. V_{obs} Max and V_{model} Max are the observed and simulated maximum velocities.

were available, and then rescaled both model-simulated and observed data using the root-square vector scale [*Chen et al*., 2016] and resampled them with 80 km resolution to make vectors in the figure visible. In the spring, the observed sea ice featured an anticyclonic drift, with a center in the Beaufort Sea and seasonally averaged maximum velocity of ~5 cm/s. This anticyclonic ice drift merged with sea ice drift in the East Siberian Sea to produce an intensified southward transpolar drift, and stronger sea ice drift velocity over the east Greenland shelf. These features were well captured by AO-FVCOM, not only in the spatial distribution but also in magnitude (Figure 5a, top plots). In the summer, the sea ice movement was characterized by a pair of anticyclonic and cyclonic drift gyres. The anticyclonic sea ice drift gyre, which was dominant in the spring, shrank significantly with its center shifting toward the Alaskan shelf. A well-defined cyclonic sea ice drift gyre was established with a center in the Eurasian Basin. A maximum drift velocity occurred between these two gyes. These double gyre structures were reasonably reproduced by the AO-FVCOM, with slight direction disparity in the cyclonic grye (Figure 5a, bottom plots). In the fall, the anticyclonic sea ice drift gyre retreated seaward, in company with the relatively weakened sea ice drift in the East Siberian Sea. During that period, the sea ice over the Chukchi shelf drifted toward the Bering Strait. These changes were also well resolved by AO-FVCOM (Figure 5b, top plots). In the winter, both observations and the model consistently showed that the anticyclonic sea ice drift grye intensified significantly, with its center migrating to the Chukchi Plateau (Figure 5b, bottom plots). The Eurasian Basin and the Barents Sea were dominated by strong cyclonic sea drift gryes, which merged with the anticyclonic sea ice drift velocity around

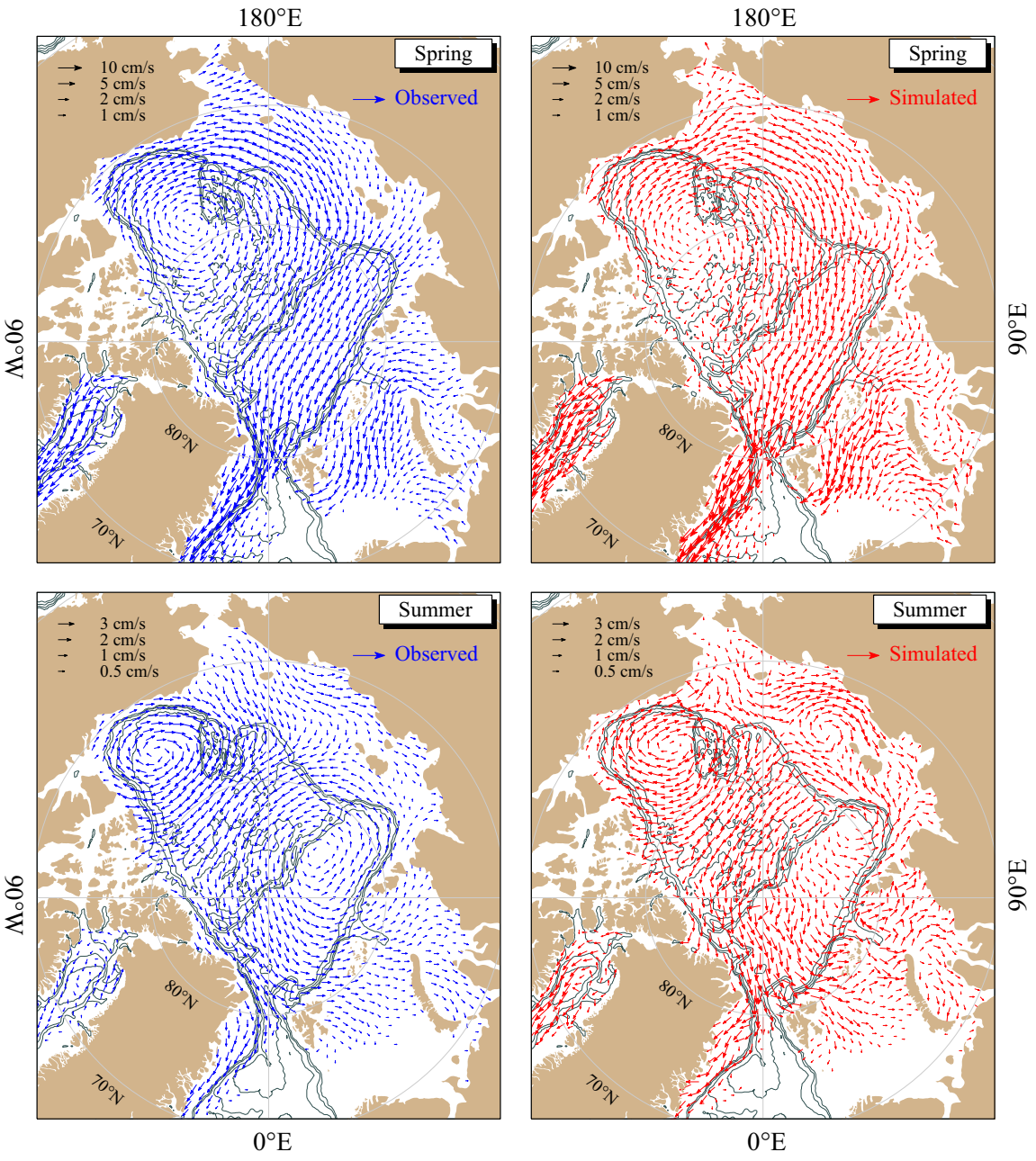

Figure 5. Comparison of model-simulated (red arrows) and observed (blue arrows) seasonal mean sea ice drift velocities averaged over the period 1979–2014. Here Figure 5a for spring and summer and Figure 5b for fall and winter.

Lomonosov Ridge to produce a strong southward sea ice drift through Fram Strait and over the eastern shelf of Greenland.

The model-produced speed and direction errors of the sea ice drift velocity varied with the wind speed (Figure 6). Over the period 1978–2014, the monthly mean wind speed averaged over the Arctic north of 70° varied in the range of 0.5–5.0 m/s, with a maximum of ~11.0 m/s at individual sites. Averaged over this region, the relationship of the model-produced sea ice drift speed error generally increased as the wind speed became stronger, as shown in Figure 6 (top plot) by the linear regression trend with a correlation coefficient of $R^2 = 0.48$. We also computed statistics at individual observational sites with a total of 5,196,226 samples over the 37 years. It showed that 68.8% was <1.0 cm/s, while 11.6%, 6.5%, 3.9%, 2.5%,

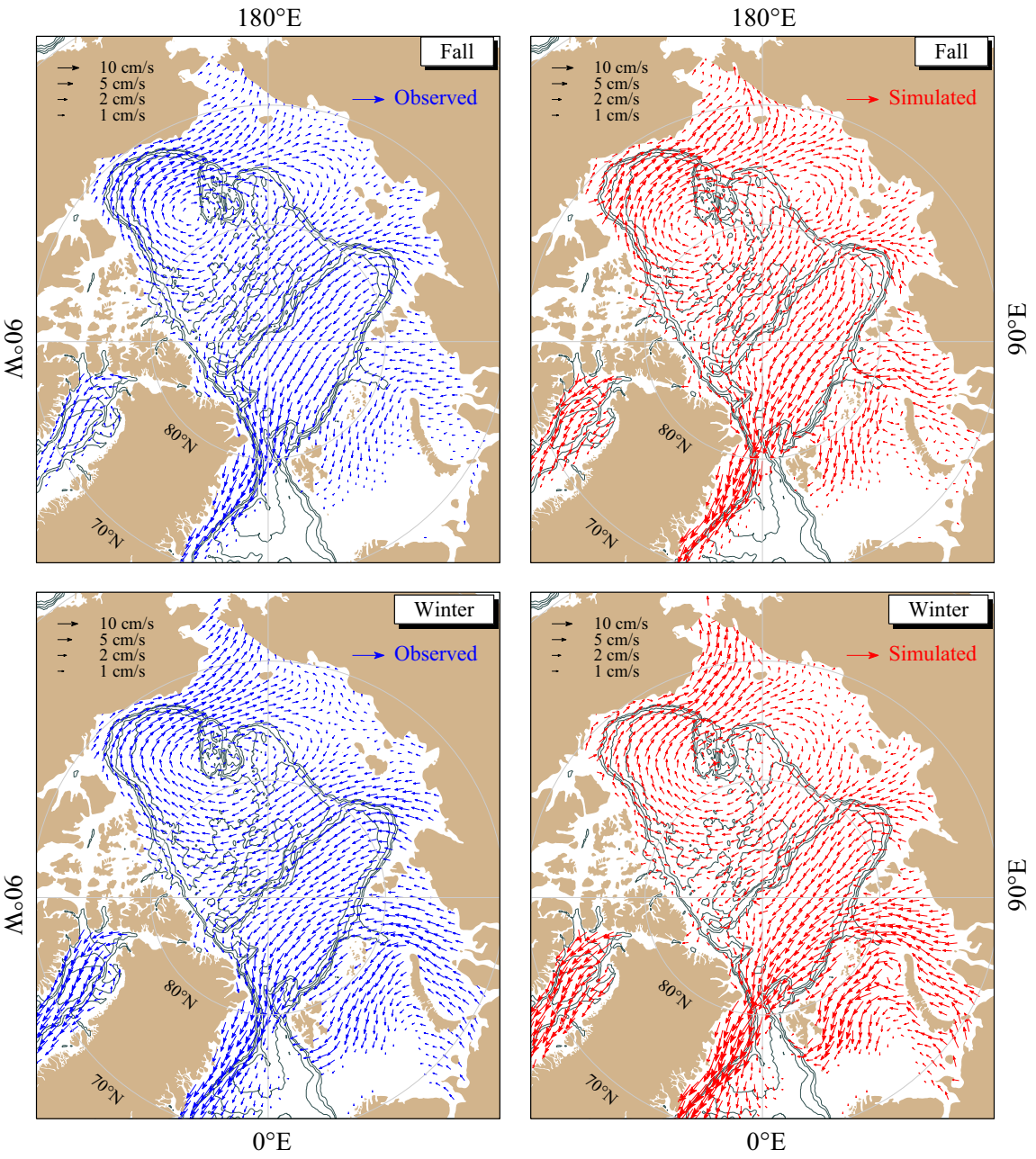

Figure 5. (Continued).

1.7%, and 1.2% were within the range of 1.0–2.0, 2.0–3.0, 3.0–4.0, 4.0–5.0, 5.0–6.0 and 6.0–7.0 cm/s, respectively. The sea ice drift speed error of >7.0 cm/s only accounted for 3.8%.

In contrast to the sea ice drift speed, the model-predicted direction error in the sea ice drift velocity generally decreased as the wind speed became stronger (Figure 6, bottom plot). The tendency was fitted well by a linear regression line with a $R^2 = 0.41$. It was consistent with the measurement uncertainty, larger in the weaker wind regime and smaller in the stronger wind regime. Statistical analysis on all samples with inclusion of sites where the observational data were available showed that 67.1% of samples had a direction error of $<30°$, with 29.7%, 22.7%, and 14.7% distributing in the direction ranges of 0°–10°, 10°–20° and 20°–30°, respectively. The direction error of $>30°$ was mainly distributed in the wind regime of <3.0 m/s.

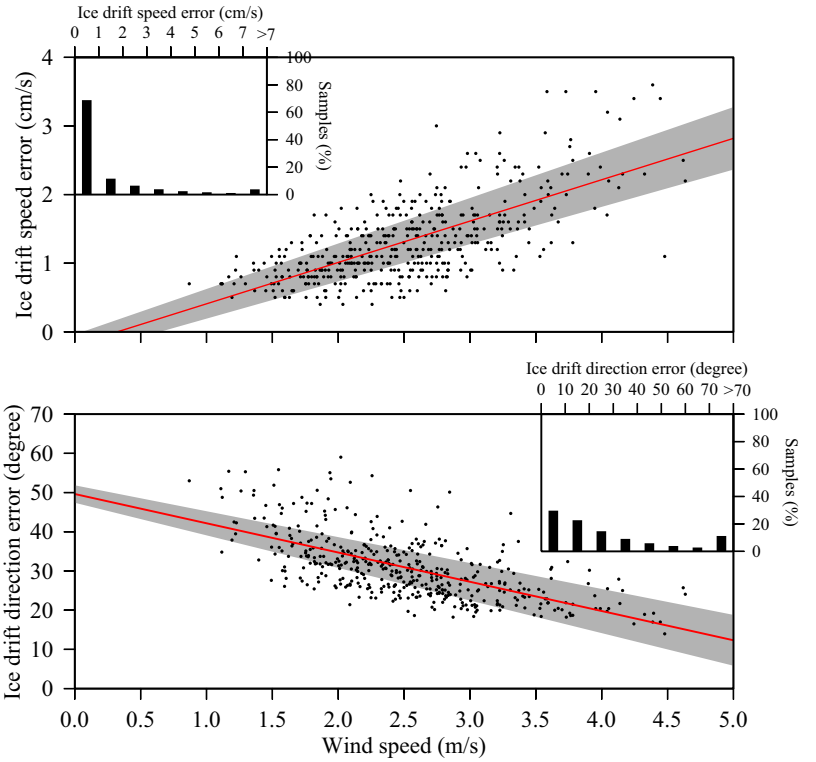

Figure 6. The relationship of model-simulated errors for sea ice drift speed and direction with surface wind speed. The spatial averaging was conducted for model and wind data in the Arctic region north of 70° for the period 1978–2014. (top) Ice drift speed error. (bottom) Ice drift direction error. Gray-shaded area indicates a 95% confidence bound of the least-square regression fit. The figures inserted in the top and bottom plot show the statistics of total individual observational samples for ice drift speed and direction errors over 1978–2014.

The reasons why the error in sea ice drift speed increased as the wind speed became larger and the error in sea ice drift direction increased when the wind speed became smaller was explored. Through the time series comparison, it was found that the larger ice drift speed errors mainly occurred in spring and winter seasons, during which there were severe storms with strong winds frequently in the Arctic Ocean. The uncertainty of the wind velocity in the CORE-v2 and NCEP was generally large during the storm events since the model generally could not accurately capture the intensity and variation of the storm-induced wind and air pressures. Therefore, the feature of sea ice drift speed errors was mainly caused by the uncertainty of the external forcing produced in the weather model. *Chen et al.* [2016] made a comparison between the AO-FVCOM-simulated and observed water velocities in the Arctic Ocean, and also found that the direction error was larger in the weak velocity zone, which was consistent with measurement uncertainties: a small error in the weak flow regime could lead to a large error in the flow direction. It was believed that their finding was also applied to the sea ice drift velocity. The small error in the satellite-derived weak sea ice drift velocity regime also could lead to a large error in the sea ice drift direction.

The simulated sea ice drift flux out of the Arctic Ocean through the major pathways was also estimated and compared with the observed data. Three sections through the Barents Sea, Fram Strait, and Bering Strait were selected (the location and length of each section are shown in Figure 1). Due to the lack of the time series of observed sea ice thickness on these three sections, the sea ice drift flux discussed here was defined as the flux per unit sea ice thickness, which was estimated by integrating the sea ice drift velocity on the section. The results showed that on the section of the Barents Sea, the simulated ice velocity flux well reproduced the observed variation, with the correlation of 0.84 with a critical value of 0.09 at a 95% significance level. However, the model generally overestimated the ice drift flux, with a relatively large mean absolute difference and RMS error of 14.33×10^3 m^2/s and 23.55×10^3 m^2/s, respectively (Figure 7, top plot). The large errors mainly occurred in winter and spring seasons, which was consistent with the finding in the comparison between the ice drift speed error and wind speed that the ice drift speed error increased as the

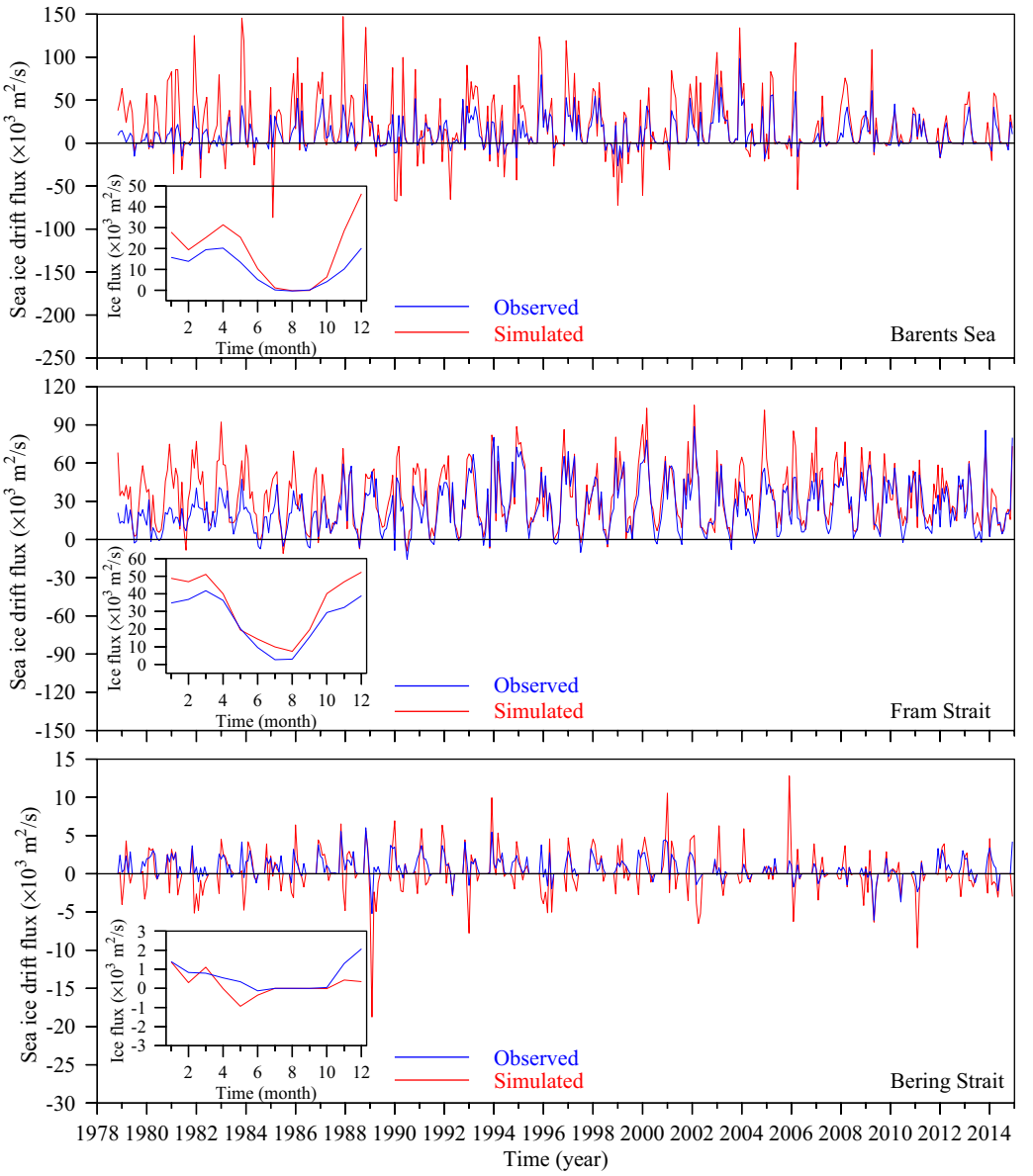

Figure 7. The comparison between simulated (red) and observed (blue) sea ice drift fluxes per unit ice thickness through the sections of the Barents Sea, Fram Strait, and Bering Strait over the period 1978–2014. The figures inserted in the plots show the simulated and observed seasonal variability of sea ice drift flux per unit ice thickness.

wind speed became larger. This also explained why it is important to improve the wind simulation in the atmospheric model. Similar results were also found in Fram Strait and Bering Strait, which showed the correlation of 0.85 and 0.62 with a critical value of 0.09 at a 95% significance level, respectively. However, the model also generally produced a larger flux, with a mean absolute difference and RMS error of 10.74 × 10^3 m^2/s and 14.44 × 10^3 m^2/s in Fram Strait (Figure 7: middle plot) and of 1.09 × 10^3 m^2/s and 2.02 × 10^3 m^2/s in Bering Strait, respectively (Figure 7: bottom plot). The monthly sea ice velocity flux anomalies through the sections of the Barents Sea, Fram Strait, and Bering Strait also captured the observed variations of the sea ice drift flux anomaly and showed relatively higher correlations of 0.83, 0.72, and 0.66 with a critical value of 0.09 at a 95% significance level, respectively (Figure 8).

The impact of the difference between simulated and observed sea ice drift patterns on the transport and distribution of sea ice was examined. The sea ice drift fluxes through these three sections were not significantly influenced by the basin-scale sea ice drift pattern. In particular for the season of summer, the major

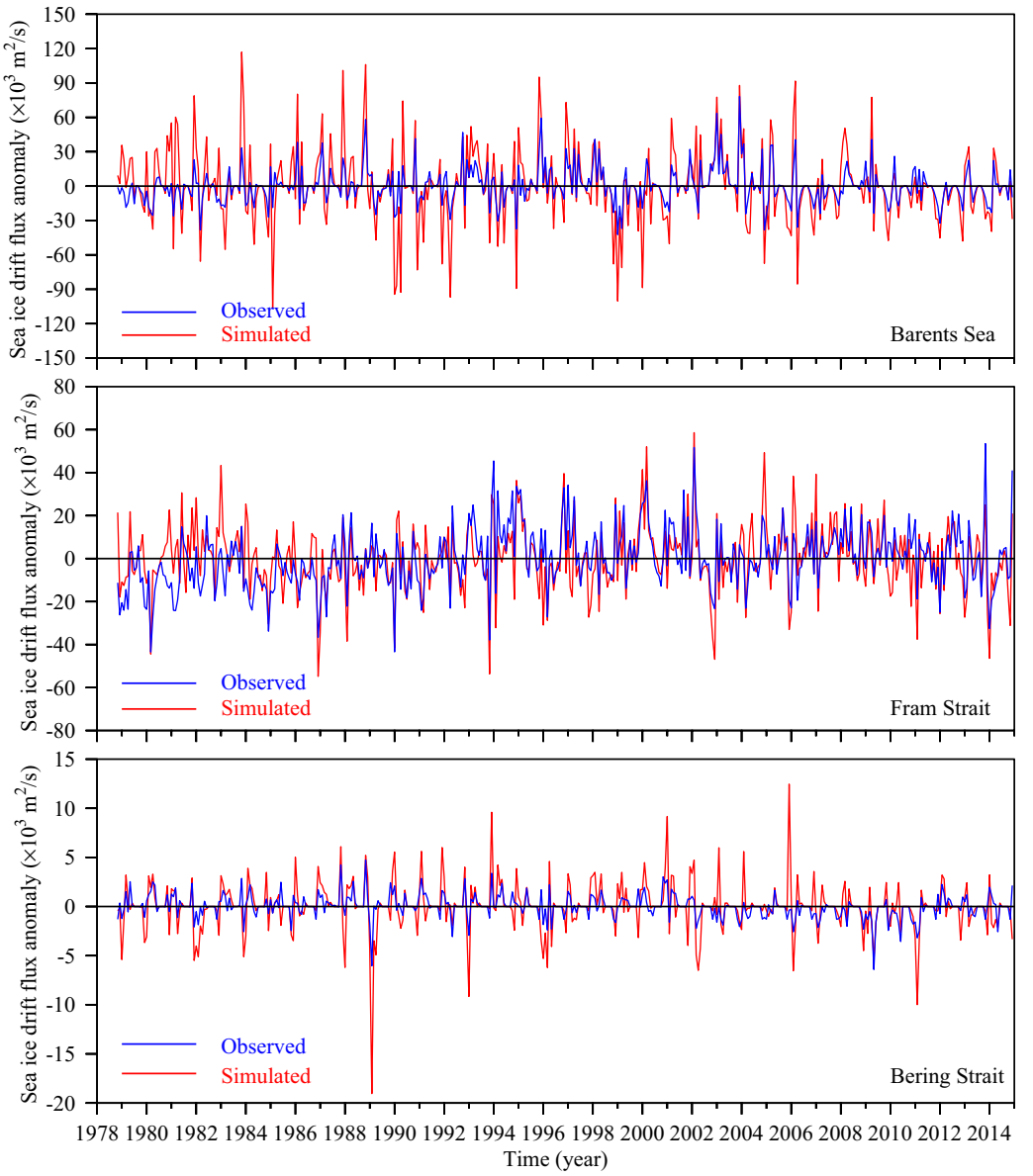

Figure 8. The comparison between simulated (red) and observed (blue) sea ice drift fluxes anomaly per unit ice thickness through the sections of the Barents Sea, Fram Strait, and Bering Strait over the period 1978–2014.

model-data discrepancy was the location of the cyclonic sea ice drift gyre: the observed cyclonic sea ice drift gyre appeared near the North Pole, while the simulated cyclonic gyre shifted farther up to the Laptev Sea. This major discrepancy had relatively little influence on the sea ice flux through the sections of the Barents Sea, Fram Strait, and Bering Strait. The overestimation of the sea ice drift flux through Fram Strait during July–August was thought to be mainly related to the overestimation of sea ice edge in Fram Strait, during which the observed sea ice drift fluxes was close to zero. The negative values found in the simulated sea ice drift fluxes through Bering Strait and the Barents Sea during April–June were believed to be mainly caused by the opposite directions found in model-simulated and observed sea ice drift velocities in the local area.

3.4. Sea Ice Thickness

Compared with the data of sea ice concentration, extent, and velocity, the measurement of the sea ice thickness remained in an insufficient monitoring status [*Johnson et al.*, 2012]. We compared model-

simulated sea ice thickness with ICESat, EM-Airborne, Romanov-Atlas, and Coastal-Stations measurement data described in section 2.2. The observed data bias significantly differed in these four kinds of data. The standard deviation of the uncertainty for the ICESat thickness data is 0.37 m [*Kwok and Rothrock*, 2009]. The uncertainty of sea ice thickness from the EM-Airborne measurements was not available, but it seemed to underestimate the mean ridge thicknesses due to the footprint and overestimate the thickness when the sensor was over the flanks of a ridge [*Haas et al*., 1997]. The uncertainties of the thickness data from Romanov-Atlas and Coastal-Stations were not available, either. *Johnson et al*. [2012] believed that those data underestimated the sea ice thickness.

Since the observed sea ice thickness used here was the monthly mean data, the model-data comparison was made by interpolating the model results at the same time onto the measurement sites and then the simulated and observed monthly means and anomalies were calculated with the same sampling numbers from the same locations. This approach was used for both spatial and time series comparisons. It was noticed that the monthly ice thickness mean produced from the ICESat campaigns was done with a varying number of daily samples since each of the campaigns had a different number of days. The comparison made by the other six numerical models also used the same approach.

For the ICESat data, the comparison was made for the distributions of ice thickness observed during 10 campaigns (Figure 9). In October–November over the period 2003–2007 (ON03–ON07), the observations showed that ice thickness exhibited a maximum of $\sim$5.0 m over the shelf connecting to the CAA and decreased toward the interior of the Arctic Basin and Russian coast (Figure 9, left column). The AO-FVCOM-simulated sea ice thickness showed the same distribution patterns as observations, although it caused an overestimation in the Canadian Basin and an underestimation in the Alaskan and Russian coastal shelf region with a difference in a range less than $\sim$1.0 m (Figure 9, second column from the left). In February–March over the period 2004–2006 and 2008 (FM04–FM06 and FM08) and also in March–April 2007 (MA07), the observed sea ice thickness showed the similar spatial distribution as those during the campaigns in October–November but was thicker on average. These features were reasonably captured by AO-FVCOM in the same error range. It was not surprising that the AO-FVCOM overestimated or underestimated the sea ice thickness since the AO-FVCOM was spun up with the idealized initial field of the sea ice consisting of five uniform categories and 2.53 m mean ice thickness in the Pan-Arctic region north of 70° [*Gao et al*., 2011]. No data assimilation was carried out to calibrate the model-produced sea ice thickness during the entire simulation period 1978–2014.

For EM-Airborne data, we calculated the observed and model-simulated monthly mean sea ice thicknesses averaged over the measurement samples over the period September 2001 to April 2009. The mean value averaged over the measurement period was 2.61 m for observations and 2.80 m for the model, with standard deviations of 1.28 and 0.96 m, respectively. The difference in the mean value was 0.19 m, an error of 7.3% relative to the observed mean value. The AO-FVCOM captured the variability of the observed anomaly of the monthly mean sea ice thickness (Figure 10). The observations showed that the sea ice thickness varied significantly with season and from year to year in the range of up to $\sim\pm$2.5 m. The observed variability in the anomaly was reproduced by AO-FVCOM except for September 2007 in which the observed anomaly value was negative, while the simulated anomaly value was positive. There were 17 samples taken on September 2007, with 13 of them taken in the Canadian Basin. We found that in the region where the September 2007 samples were taken, the sea ice thickness was overestimated by the AO-FVCOM during that month. This was the reason why the model produced a positive anomaly for that month. The mean absolute difference and RMS error between simulated and observed sea ice thickness anomalies were 0.54 and 0.69 m, respectively, with a minimum difference of 0.03 m and a maximum difference of 1.74 m.

For the Romanov-Atlas data set, the measurements were made in March–May each year covering a 12 year period from 1978 to 1989. The 12 year mean sea ice thickness averaged over all measurement sites was 1.80 m for observations and 2.70 m for the model, with standard deviations of 0.47 m for both the observations and model. The model-simulated and observed monthly anomalies of the sea ice thickness agreed well, showing a correlation coefficient of 0.79 with a critical value of 0.35 at a 95% significance level (Figure 11). The difference between model-simulated and observed monthly anomalies was in the range of 0.04–0.69 m, with a mean absolute difference mean and RMS error of 0.24 and 0.30 m, respectively. The major difference mainly happened in March–May, 1986, during which the observed anomaly was negative but the model-simulated anomaly was positive.

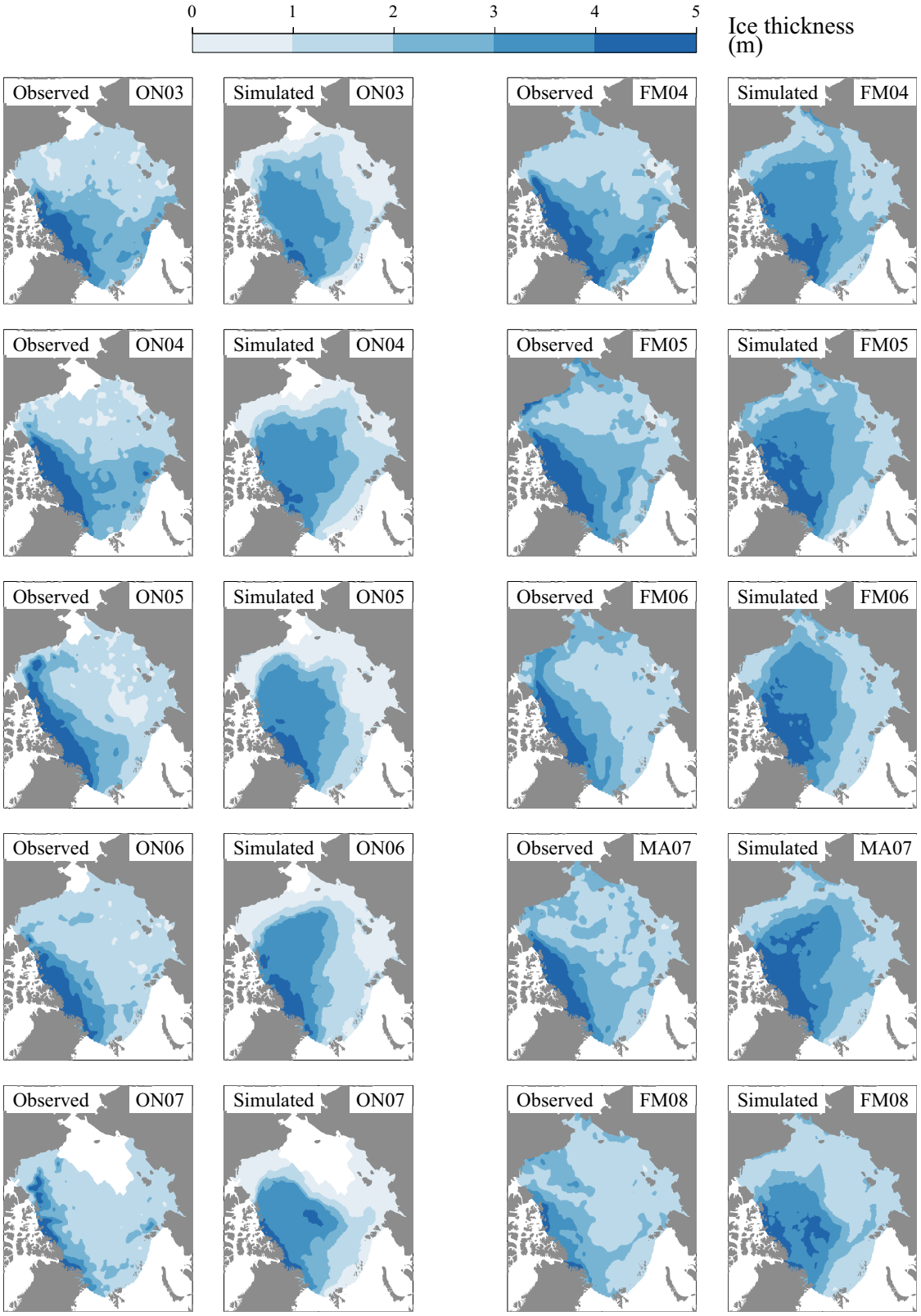

Figure 9. Comparison of the spatial distributions of the simulated and observed ice thicknesses taken in the 10 ICESat campaigns during fall and winter seasons. Labels ON, FM, and MA denote October–November, February–March, and March–April, respectively.

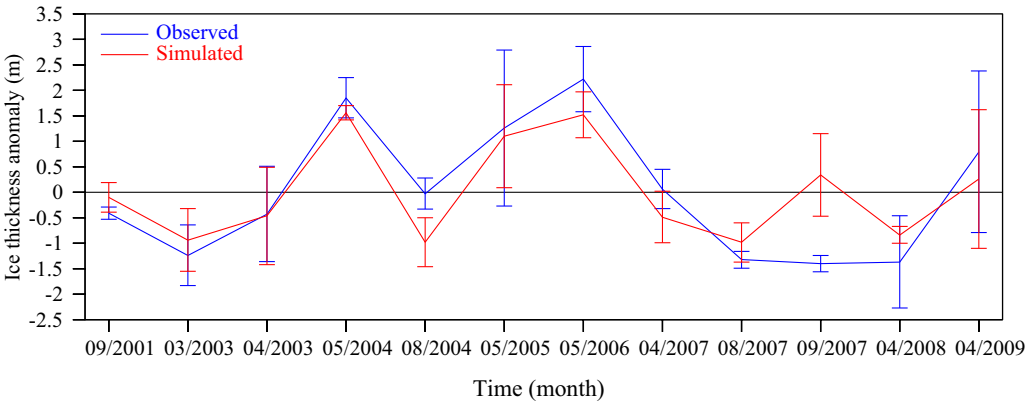

Figure 10. Comparison of the simulated monthly ice thickness anomaly with the observed data collected from the EM-Airborne measurements. Both model and observational data were averaged over the measurement samples. The vertical bars are the standard deviations derived by spatially averaging simulated (red) and observed (blue) monthly data.

For the Coastal-Stations data set, the year-through measurements were made at 50 coastal stations over the period 1998–2008. The comparison was made for monthly and yearly mean sea ice thickness averaged over these stations (Figure 12). The observed and model-simulated monthly mean ice thicknesses were 0.52 and 0.64 m, with standard deviations of 0.37 and 0.48 m, respectively. The anomaly of the model-simulated sea ice thickness matched reasonably with the observed anomaly, not only in phase but also in amplitude (Figure 12, top plot). The correlation coefficient between these two anomaly time series was 0.95, with a critical value of 0.17 at a 95% significance level. Their difference was in the range of 0.01–0.50 m, with the mean absolute difference mean and RMS error of 0.14 and 0.17 m, respectively. The AO-FVCOM captured the observed annual cycle of the anomaly of the sea ice thickness, minimum occurring in September, and maximum occurring during April–May. Both observed and model-simulated annual-mean sea ice thickness anomalies averaged over those 50 coastal stations exhibited a small interannual variability along the Russian coast. The variability was in the range of 0.01–0.10 m, with the mean absolute difference and RMS error of 0.04 and 0.05 m, respectively (Figure 12, bottom plot). Although the annual mean averaged over those stations was small, both the observation and model showed that the anomaly of the sea ice thickness varied significantly from station to station, which was evident in a relatively large mean standard deviation of ~0.4 m shown in Figure 12 (bottom plot).

4. Comparisons With Six Other Numerical Models

We added AO-FVCOM sea ice simulation results to the model-data comparison that was made by *Johnson et al.* [2012] for six other models: (1) ECCO2, (2) GSFC, (3) INMOM, (4) ORCA, (5) NAME, and (6) UW. The

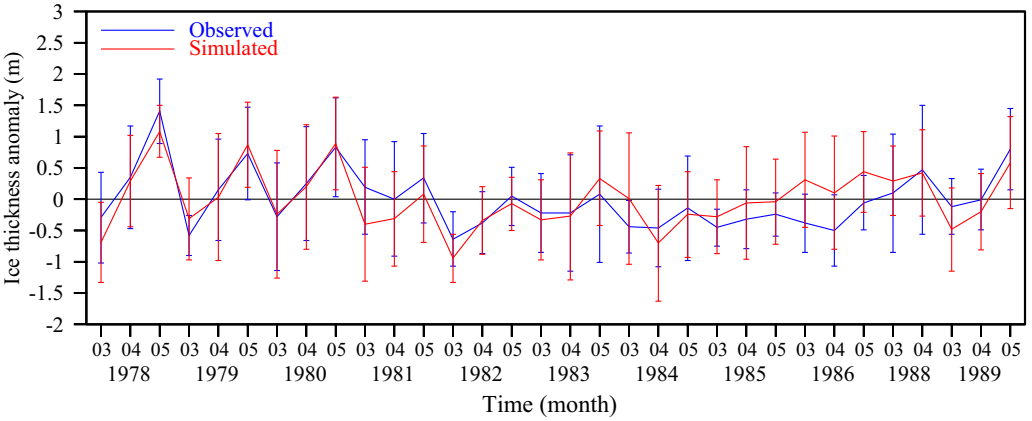

Figure 11. Comparison of the simulated and observed monthly ice thickness anomalies averaged over the sites of the Romanov-Atlas. The vertical bars are the standard deviations estimated by averaging simulated (red) and observed (blue) monthly data at the sites.

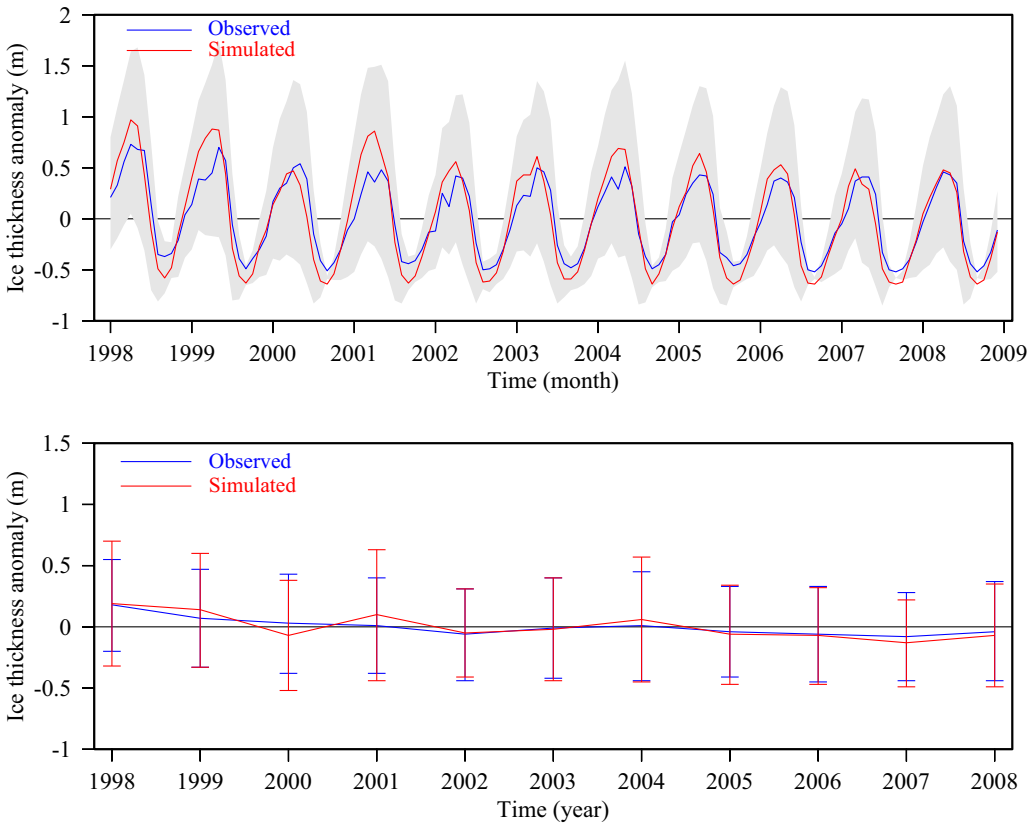

Figure 12. Comparison of the simulated and observed monthly and yearly ice thickness anomalies averaged from 50 coastal stations. (top) Monthly averaged; (bottom) Yearly averaged. Gray-shaded area indicates the mean standard deviation averaged from simulated and observed monthly standard deviations. Vertical bars are the standard deviations estimated from the yearly data of 50 stations for the simulated (red) and observed (blue) data.

ECCO2 was configured using the Massachusetts Institute of Technology general circulation model (MITgcm) with a resolution of 15–22 km in the horizontal and 50 z-levels in the vertical [*Marshall et al*., 1997; *Losch et al*., 2010; *Nguyen et al*., 2011]. The GSFC was configured using the Princeton Ocean Model (POM) with a horizontal resolution of 0.35–0.45° and 26 vertical z-levels [*Blumberg and Mellor*, 1987; *Mellor et al*., 2002]. The INMOM was configured using the Institute of Numerical Mathematics Climate Model (INMCM) from the Russian Academy of Science with a horizontal resolution of 0.25° and 27 vertical sigma-levels [*Volodin et al*., 2010]. The ORCA was configured using the Nucleus for European Modelling of the Ocean (NEMO) with a horizontal resolution of ∼3–6 km and 64 vertical z-levels [*Madec*, 2008]. The NAME was configured using the Parallel Ocean Program (POP) with a horizontal resolution of ∼9 km and 45 vertical z-levels [*Smith et al*., 1992; *Maslowski et al*., 2004]. The UW model was configured using the global parallel ocean and ice model (POIM) with a horizontal resolution of 6–75 km and 30 vertical z-levels [*Zhang and Rothrock*, 2003].

Johnson et al. [2012] used Taylor diagrams [*Taylor*, 2001] to illustrate quantitative assessment of the six model performance through the comparison with the observed sea ice thickness. The Taylor diagram displays the statistics of synthesis analysis, with the residuals defined as the difference of simulation minus observation and model-data correlation coefficient computed according to the record length. The residual is presented by the radial circle with ± 2 m corresponding to $\pm\pi$ in angle. The correlation coefficient is indicated by the distance from the origin (defined as 0) with a maximum of 1.0. This method has been widely used in evaluating model performances via observations [e.g., *Tian et al*., 2015]. We adopted it here to be consistent with *Johnson et al*. [2012].

The Taylor diagram comparison was performed for four types of sea ice thickness data from ICESat, EM-Airborne, Romanov-Atlas, and Coastal-Stations. For the ICESat campaigns, ORCA was not available, so comparison of AO-FVCOM was made with the other five models, and results are displayed in Figure 13a. The

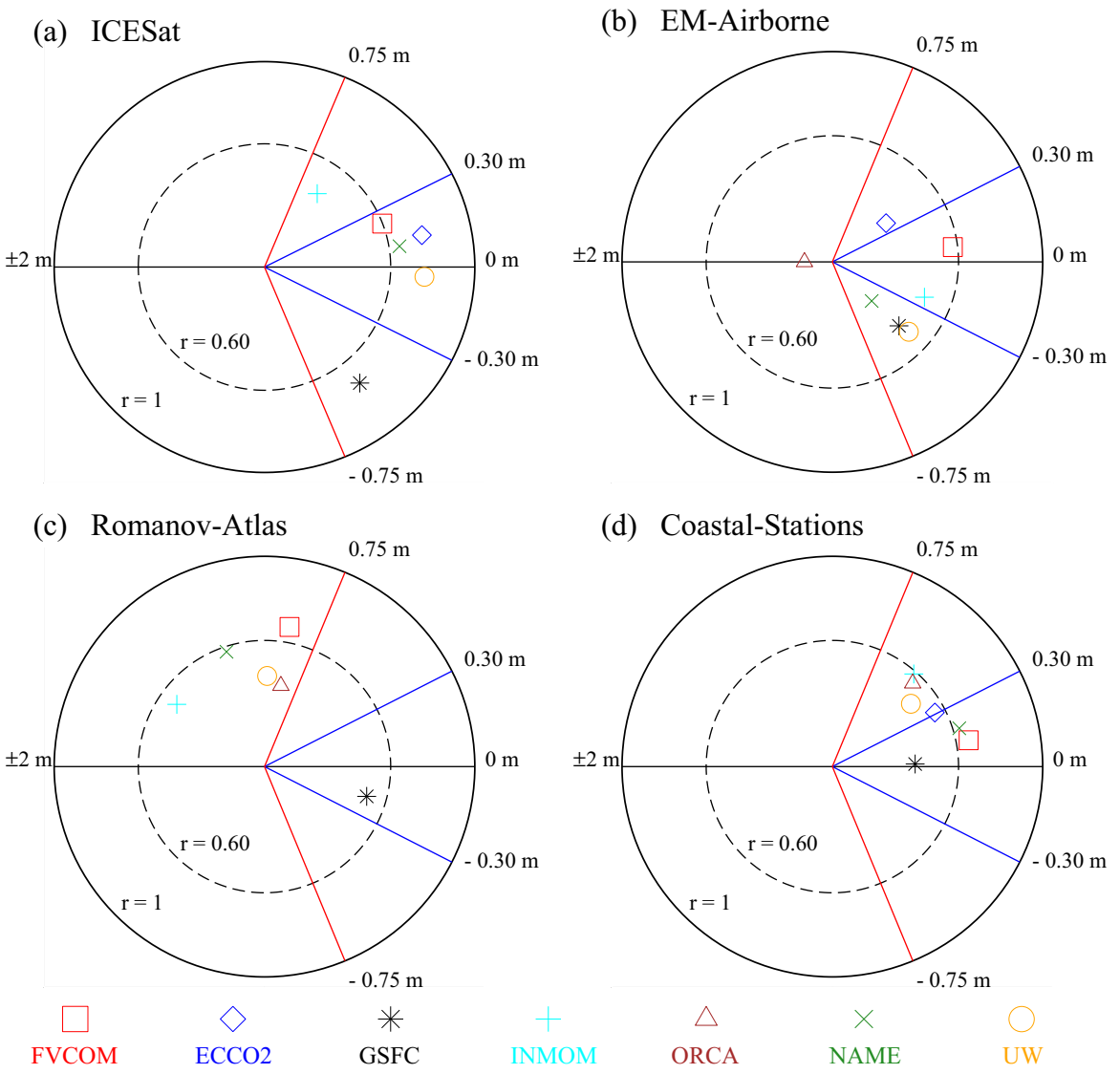

Figure 13. Taylor diagrams showing correlation coefficients and residuals for the seven models. Here (a) ICESat campaigns (ICESat), (b) electromagnetic airborne data (EM-Airborne), (c) Romanov Atlas (Romanov-Atlas), and (d) 51 coastal stations (Coastal-Stations).

residuals and correlation coefficients in that diagram for the AO-FVCOM were averaged from the yearly mean results over the period 2003–2008. Like ECCO2, NAME, and UW, the AO-FVCOM showed a correlation coefficient of 0.60 and a residual with an absolute value of $<$0.30 m, while, as pointed out by *Johnson et al.* [2012], the GSFC produced a larger residual of $-$0.57 m, though its correlation coefficient was above 0.60, and the INMOM had the largest residual of 0.61 m and lowest correlation coefficients of 0.44. It should be noticed that as each model was run with different simulated periods at the time that the comparison was made by *Johnson et al.* [2012] so that the multiyear mean of correlation coefficients and residuals from those models were averaged over different years. The ECCO2, GSFC, UW, and AO-FVCOM were averaged over 2003–2008, INMOM was over 2003–2006, and NAME was only over 2003–2004. We also calculated residual and correlation coefficient over different lengths of years for AO-FVCOM, and the resulting correlation coefficients and residuals were 0.62 and 0.16 m as the same case as INMOM and 0.72 and 0.11 m as the same case with NAME. The AO-FVCOM retained the same correlation coefficient level but smaller residuals as the time length used for the average was shortened.

For the EM-Airborne data, the AO-FVCOM showed the highest correlation of 0.58, and other six models all had values less than 0.50 (Figure 13b). The AO-FVCOM produced the lowest residual value of 0.08 m, while

the INMOM was −0.23 m, ECCO2 was 0.40 m, GSFC was −0.49 m, NAME was −0.50 m, and UW was −0.47 m. The ORCA-produced residual was ∼2.10 m, out of the plotting limitation of ±2.00 m (Figure 13b). Similar to the ICESat data comparison, the residuals and correlation coefficients for models were estimated over different time lengths. The AO-FVCOM and GSFC used the 8 year data covering the period 2001–2009; the ECCO2 and UW used the 7 year data covering the period 2001–2008; the INMOM used the 5 year data covering the period 2001–2006; the NAME used the 3 year data covering the period 2001–2004; and the ORCA only used the 1 year data from 2001. We recalculated the correlation coefficient and residual for AO-FVCOM based on the different time lengths used in these models. The resulting correlation coefficient and residual were 0.53 and 0.14 m for a 7 year averaging, 0.74 and 0.01 m for a 5 year averaging, 0.73 and 0.17 m for a 3 year averaging, and 0.49 and 0.5 m for a 1 year averaging.

For the Romanov-Atlas data, the comparison was made between AO-FVCOM and the other five model excluding ECCO2 (the model data were not available at the time *Johnson et al*. [2012]'s analysis was conducted). For all models, the correlation coefficients and residuals were estimated by averaging over the period 1978–1989. The AO-FVCOM produced the highest correlation coefficient of 0.67. The GSFC, INMOM, and NAME also showed relatively high correlation coefficients in the range of 0.50–0.60, while the UW and ORCA had values of ∼0.40. The residuals produced by AO-FVCOM, INMOM, ORCA, NAME, and UW were above 0.75 m, and only GSFC had a negative residual of about −0.18 m.

For the Coastal-Stations data, the correlation coefficients and residuals were averaged over monitoring stations covering the period 1998–2008. The AO-FVCOM produced the highest correlation coefficient of 0.66, which was slightly higher than, but not significantly different from, the value of 0.63 estimated by NAME. The correlation coefficients estimated by ECCO2, INMOM, ORCA, and UW were in the range of ∼0.45–0.60, while the GSFC showed the lowest correlation of 0.39. The GSFC produced the smallest residual with a value of 0.02 m. The residual estimated by AO-FVCOM was 0.12 m, which was higher than GSFC, similar to the value of 0.19 m estimated by NAME, and lower than the values of ∼0.30–0.55 m shown in ECCO2, INMOM, ORCA, and UW. It should be noticed that different numbers of stations were selected for averaging in different models. The AO-FVCOM, NAME, and INMOM included 50 stations (one station was in the inland region which was not resolved). The ECCO2 included 51 stations, while GSFC, UW, and ORCA used 38, 36, and 21 stations, respectively. Since no information was provided for particular stations that were selected for different models, we were not able to conduct a further comparison using the same stations as those models.

To assess the capability of models to capture the spatial distribution of the sea ice thickness, *Johnson et al*. [2012] also included figures showing the comparison of the 5 year (1982–1986) averaged distributions of observed and model-simulated sea ice thicknesses in the Siberian Seas (the Chukchi, East Siberian, Laptev, and Kara Seas) based on the Romanov-Atlas measurement data set. We include the same type of comparison for AO-FVCOM in Figure 14. The AO-FVCOM produced the same spatial distribution as the observations, with a maximum sea ice thickness in the East Siberian Sea. Except for the GSFC, the INMOM, ORCA, NAME, and UW also showed similar spatial distribution patterns as AO-FVCOM with positive residuals in most areas (see Figure 4 in *Johnson et al*. [2012]). In addition to these consistencies, the residuals of the sea ice thickness predicted by models were diverse in detail. The AO-FVCOM was consistent with UW and ORCA, showing that the smallest (near-zero residual) errors occurred in some coastal areas of the Laptev Sea and Kara Sea. The NAME-predicted smallest errors occurred in the Laptev Sea and Karea Sea but the areas were smaller. In addition to the Laptev and Kara Seas, the UW and ORCA also predicted the near-zero residual area in the East Siberian Sea. The INMOM exhibited a relatively larger positive residual over the entire observational domain. In contrast to all other models, the GSFC produced a negative residual in the Laptev Sea and Kara Sea, and had near-zero residuals in the marginal zones in the East Siberian Sea. A detailed discusson for the six model performances were given in *Johnson et al*. [2012], and we will give a brief summary here.

5. Discussion

Similar to all other Arctic Ocean models, the AO-FVCOM also produced relatively large errors in the direction of the sea ice drift velocity with a general mean uncertainty of ∼30° in the region north of 70°. We believe that this is partially related to the measurement uncertainty. However, since there was no measurement

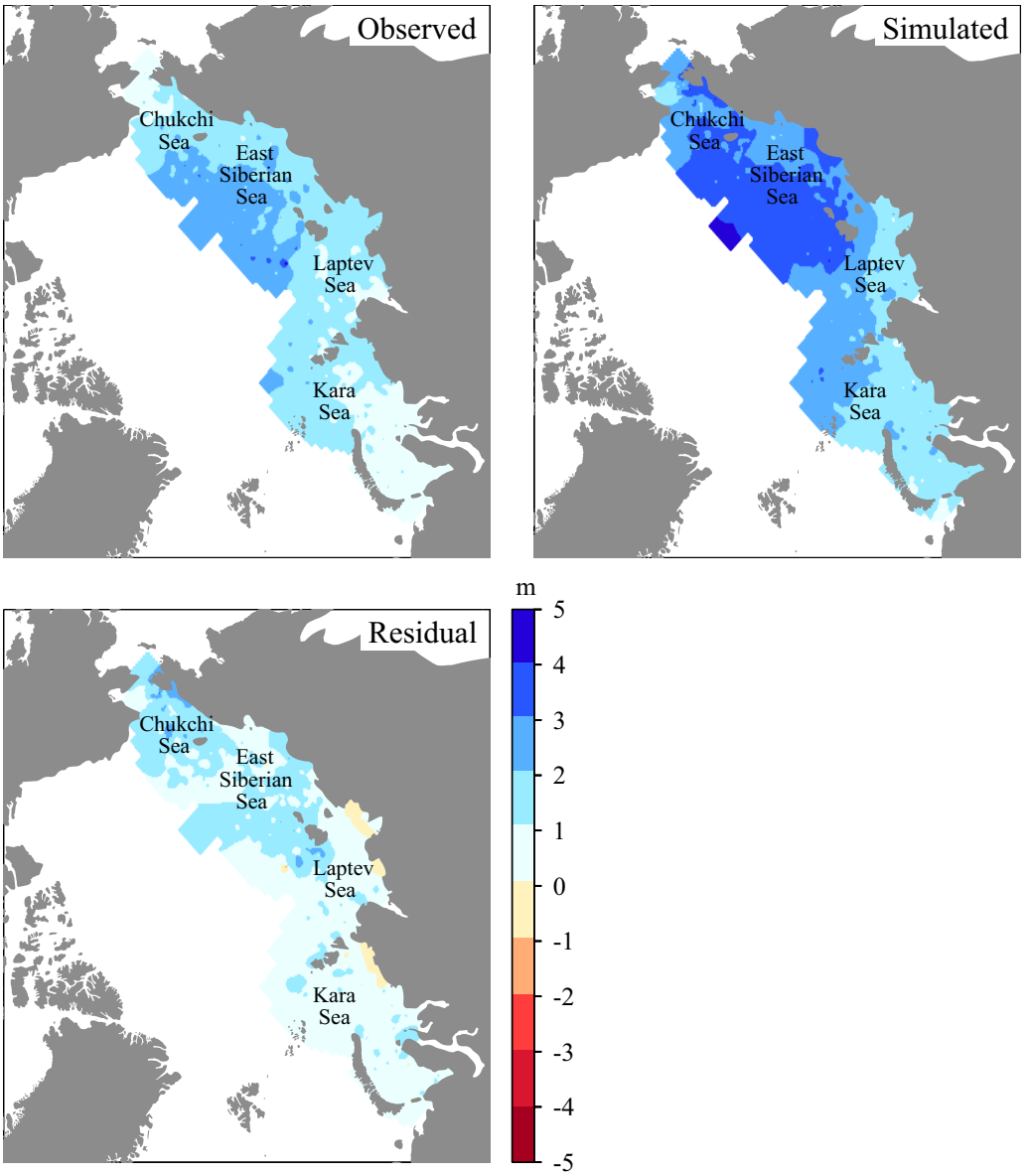

Figure 14. Comparison between the distributions of observed and simulated ice thicknesses averaged over the period 1982–1986 during which the Romanov-Atlas measurements were made. (left: top) Observed; (right: top) Simulated; and (left: bottom) the model-data difference.

uncertainty estimation available with the sea ice drift velocity data, we were not able to judge if the model-data difference was due to measurement uncertainty. The fact is that the largest differences usually occurred in the marginal ice zones in all years, suggested that it is related to the model skill and performance in simulating the ice-drift velocity in the region where it was not fully covered by sea ice. *Martin et al.* [2014] examined the dependence of the wind-induced momentum flux to the ocean on the sea ice concentration, finding that the maximum flux occurred at a sea ice concentration of 0.8–0.9. In the fully sea-ice coupled system, in turn, it could affect the ice movement floating in the water. *Martin et al.* [2016] conducted a further analysis based on model experiments, suggesting that the varying sea ice drag coefficient could have a significant impact on the ocean surface stress and thus influence the seasonal and interannual variability of the sea ice in the Arctic Ocean. To examine the impact of the parameterization in the surface forcing on the sea ice simulation, we also conducted a series of sensitivity experiments using various surface drag coefficients and turning angles for the year 2007. This year was selected since the observed yearly mean ice drift velocity was the largest compared with all other years.

The surface stress consists of three components: the wind stress onto the sea ice ($\vec{\tau}_{ai}$), the water stress at the ice-sea interface ($\vec{\tau}_{wi}$), and the internal stress tensor (σ_{ij}). Here subscripts $i = 1, 2$ and $j = 1, 2$ represent x- (noted as "1") and y- (noted as "2") components of σ. In the UG-CICE, σ_{ij} is determined with the inclusion of Elastic-Viscous-Plastic (EVP) dynamics, while $\vec{\tau}_{ai}$ and $\vec{\tau}_{wi}$ are calculated by the empirical formula given as

$$\vec{\tau}_{ai} = cC_{ai}\rho_a|\vec{u}_a|\left(\vec{u}_a cos\varphi + \vec{k}\times\vec{u}_a sin\varphi\right) \tag{3}$$

$$\vec{\tau}_{wi} = cC_{wi}\rho_w|\vec{u}_w - \vec{u}_i|(\vec{u}_w - \vec{u}_i)cos\theta + \vec{k}\times(\vec{u}_w - \vec{u}_i)sin\theta) \tag{4}$$

where c is the ice concentration; $\vec{u}_a$, $\vec{u}_w$, and $\vec{u}_i$ are the surface wind, surface water, and ice velocity vectors; C_{ai} and C_{wi} are the air and water drag coefficients; ρ_a and ρ_w are the air and water densities; and φ and θ are the air and water turning angles. In the 37 year simulation, C_{ai} and C_{wi} were parameterized by

$$C_{ai} = (1.1 + 0.04|\vec{u}_a|)\times 10^{-3} \tag{5}$$

and $C_{wi} = 5.5\times 10^{-0}$. φ was specified by

$$\varphi = \begin{cases} 30^\circ, & \text{for } |\vec{u}_a| < 15 \text{ m/s} \\ 20^\circ, & \text{for } |\vec{u}_a| \geq 15 \text{ m/s} \end{cases} \tag{6}$$

and $\theta = 25^\circ$.

We have made two experiments (hereafter referred to as Exp#1 and Exp#2) in the region north of 70°N. Exp#1 was designed to examine the sensitivity of model-simulated sea ice drift speed and direction to C_{ai} and φ. In this experiment, we ran the model for seven cases. Case 1 was for C_{ai}, in which a constant value of 1.3×10^{-3} from *Martin et al.* [2016] was used instead of the function with wind speed used in our simulation. Cases 2–7 were for φ, in which we ran the model using φ values of 0°, 10°, 20°, 30°, 40°, and 50°. Exp#2 was designed to examine the parameterization for C_{wi} and θ. In this experiment, we ran the model for four cases. Cases 1 and 2 were for C_{wi}, in which we ran the model by increasing and decreasing C_{wi} values by 10% to 6.05×10^{-3} and 4.95×10^{-3}, respectively. Cases 3 and 4 were for θ, in which the model was run by increasing and decreasing θ values by 10° to 35° and 15°, respectively. We defined the year 2007 model run with the same parameters used for the 37 year simulation as "simulation," and compared all different cases with this "simulation" case.

For Exp#1, the comparisons were made based on monthly and yearly mean errors. The monthly mean error was estimated by first calculating monthly mean of the absolute difference at individual grid nodes and then conducting the spatial mean including all grid nodes. The yearly mean error was defined as the mean of monthly mean errors averaged over 12 months. The percentage value used in the sea ice speed comparison is defined as the ratio of the difference between the experimental case and the "simulation" case to the yearly mean observed sea ice drift velocity. For Case 1, we found that using a constant C_{ai} reduced the ice drift speed error by ~5.9%, but not always the direction error (Figure 15). The ice drift direction error became larger in January–June, August, October–December, and reduced in July and September, with yearly mean and RMS errors increasing by ~0.7° and ~0.6°, respectively (Table 2). For Cases 2–7, we found that both ice drift speed and direction errors showed similar monthly variation patterns as the "simulation," but mean absolute and RMS errors differed significantly from case to case. The sea ice drift speed mean absolute errors remained unchanged for Cases 2–5, but decreased by ~2.9% for Cases 6–7 (Table 2). The RMS ice drift speed errors remained unchanged for Case 2 and 5–6, increased by ~2.9% for Case 3–4 and decreased by ~5.9% for Case 7. Similar to Case 1, the direction errors also varied significantly with time. The direction errors for Cases 3–5 with φ values of 10°, 20°, and 30° were similar to that obtained from the "simulation" case: noticeably smaller in Case 4 (−0.6°), slightly larger in Case 3 (0.3°), and equally in Case 5. The direction errors for Case 2 and Cases 6–7 were significantly larger, with the yearly mean error difference in the range of 2.3–7.1° (Table 2). Cases 6–7 tended to produce a larger direction error as φ increased, with a maximum up to ~11.7° occurring in November with φ of 50° (Figure 15). Overall, the air-ice drag coefficient and turning angle specified for our 37 year simulation were robust regarding the error analysis in ice speed and direction, although we found that either a constant air-ice drag coefficient of 1.3×10^{-3} or a fixed turning angle of 20° could slightly improve the model performance in the ice drift speed or direction simulation.

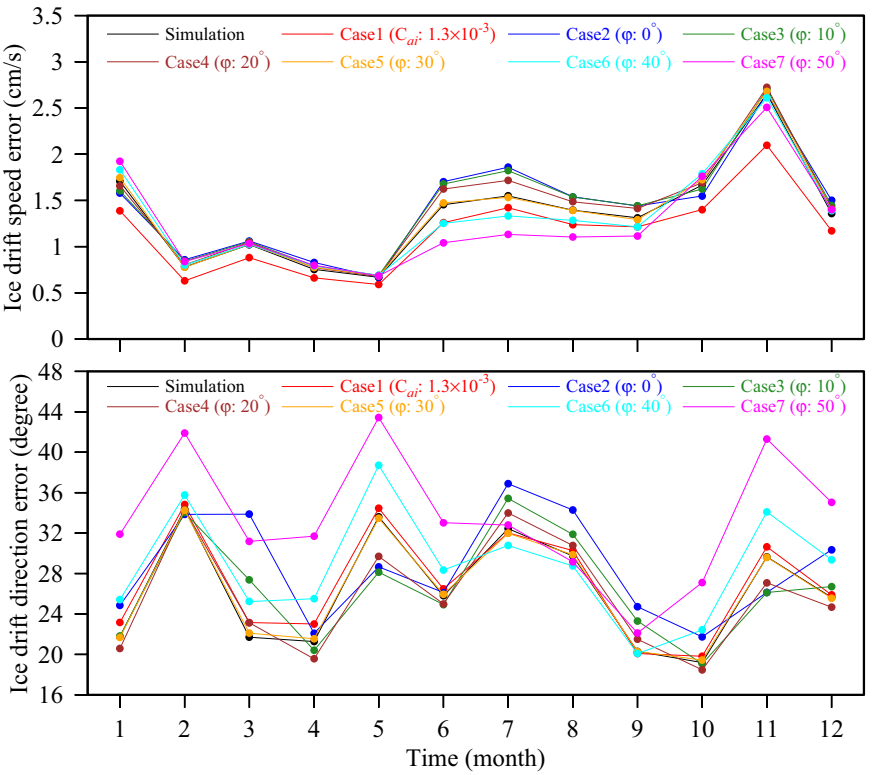

Figure 15. Comparisons of model-produced monthly mean errors of the absolute model-data difference for Cases 1-7 in Exp#1. (top) Ice drift speed error. (bottom) Ice drift direction error.

The impacts of the air and water drag coefficients and turning angles on the sea ice concentration and extent were further estimated. In all Cases 1–7 of Exp#1, the influences of the air drag coefficients and turning angles on the sea ice concentration were very slight. Case 1 only reduced the bias of sea ice concentration by 0.1% for mean absolute difference, with an increase of the RMS error by 0.3% (Table 2). Cases 2–4 decreased the bias by 0.7% and 0.6%, 1.0%, and 0.8%, and 0.7% and 0.6% for mean absolute differences and RMS errors, respectively. Case 5–7 increased the bias of sea ice concentration by 0.1% and 0.1%, 1.4% and 1.2%, and 2.7% and 2.3% for mean absolute differences and RMS errors, respectively.

The sensitivities of the sea ice extent to the parameterizations in Exp#1 were relatively larger than that on the sea ice concentration. Cases 1 using a constant C_{ai} could decrease the model-data bias of the sea ice extent by 4.9% in mean absolute difference and 11.1% in the RMS error (Table 2). In Cases 2–4, however, the mean absolute difference and RMS errors were increased by 6.8% and 19.1%, 4.1% and 13.2%, and 1.2%

Table 2. Comparison of Yearly Mean Sea Ice Speed, Direction, Concentration, and Extent Error Differences for 2007 Between Cases 1–7 and "Simulation" in Exp#1[a]

Cases	|ΔV| (cm/s)	ΔV RMS (cm/s)	|Δα| (°)	Δα RMS (°)	|ΔCon| (×10^{-4})	ΔCon RMS (×10^{-4})	|ΔExt| (×10^4 km^2)	ΔExt RMS (×10^4 km^2)
C_{ai}: 1.3 × 10^{-3}	−0.2	−0.4	0.7	0.6	−1.6	5.5	−1.5	−4.5
φ: 0°	0.0	0.0	2.3	2.2	−8.2	−12.1	2.1	7.8
φ: 10°	0.0	0.1	0.3	0.4	−12.1	−16.5	1.2	5.4
φ: 20°	0.0	0.1	−0.6	−0.5	−8.2	−13.2	0.4	2.2
φ: 30°	0.0	0.0	0.0	−0.1	0.6	3.0	0.3	−0.2
φ: 40°	−0.1	0.0	2.4	1.9	17.8	26.6	−0.5	−3.6
φ: 50°	−0.1	−0.2	7.1	6.3	33.7	49.4	−1.3	−5.2

[a]Note: |ΔCon| and ΔCon RMS represent the mean absolute differences and root mean square differences of the sea ice concentration between the observation and model. |ΔExt| and ΔExt RMS represent the mean absolute differences and root mean square differences of the sea ice extent between the observation and model. The positive and negative signs indicate Cases 1–7 producing larger and smaller error than the "simulation," respectively.

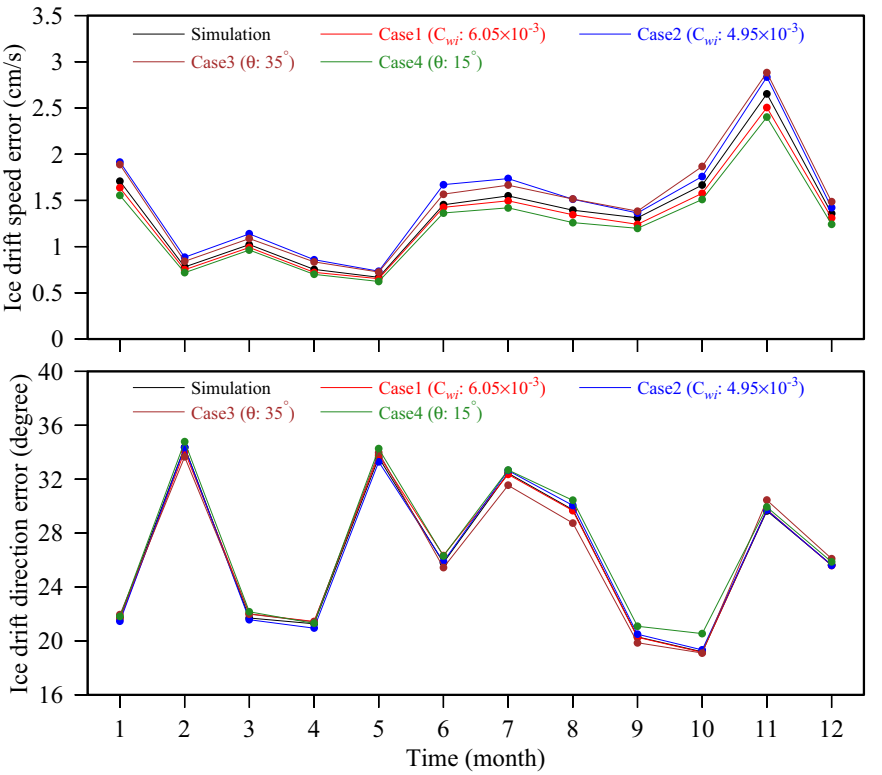

Figure 16. Comparisons of model-produced monthly mean errors of the absolute model-data difference for Cases 1-4 in Exp#2. (top) Ice drift speed error. (bottom) Ice drift direction error.

and 5.3%, respectively. In Case 5, the mean absolute difference was increased by 1.0% and the RMS error was decreased by 0.5%. Cases 6–7 were similar to Case 1, which helped to reduce the mean absolute differences by 1.6% and 4.3% and the RMS errors by 8.8% and 12.8%, respectively.

For Exp#2, we found that changing either C_{wi} by 10% or θ by 10° did not show a significant change in the temporal variation and value of model-produced ice drift velocity error (Figure 16). For Case 1, increasing C_{wi} by 10% only reduced the ice drift speed error by ∼2.9%, but the ice drift direction error remained unchanged (Table 3). For Case 2, decreasing C_{wi} by 10% enlarged the ice drift speed error by ∼2.9%, but the ice drift direction error remained unchanged. Therefore, for a given θ, the impact of changing C_{wi} on the ice drift velocity was mainly in the ice drift speed but not in the ice drift direction. For Case 3, increasing θ by 10° enlarged the sea ice drift speed error by ∼2.9% but slightly reduced the sea ice direction error by ∼0.1° (Table 3). In contrast, for Case 4, decreasing θ by 10° reduced the sea ice drift speed error by ∼5.9% but increased the ice drift direction error by ∼0.5°. Overall, based on the four cases, we found that the sea ice drift speed was more sensitive to the change of C_{wi} and θ than the sea ice drift direction. The parameters of C_{wi} and θ specified for our 37 year simulation run were robust.

Table 3. Comparison of Yearly Mean Sea Ice Speed, Direction, Concentration, and Extent Error Differences for 2007 Between Cases 1–4 and "Simulation" in Exp#2[a]

Cases	|ΔV| (cm/s)	ΔV RMS (cm/s)	|Δα| (°)	Δα RMS (°)	|ΔCon| (×10^{-4})	ΔCon RMS (×10^{-4})	|ΔExt| (×10^4 km^2)	ΔExt RMS (×10^4 km^2)
C_{wi}: 6.05 × 10^{-3}	−0.1	−0.1	0.0	0.0	−5.5	−6.8	−0.8	−2.0
C_{wi}: 4.95 × 10^{-3}	0.1	0.2	0.0	−0.1	8.1	9.0	1.5	3.8
θ: 35°	0.1	0.2	−0.1	−0.5	10.6	17.6	0.3	0.8
θ: 15°	−0.2	−0.2	0.5	0.8	0.7	−2.5	−0.7	−1.3

[a]Note: |ΔCon| and ΔCon RMS represent the mean absolute differences and root mean square differences of the sea ice concentration between the observation and model. |ΔExt| and ΔExt RMS represent the mean absolute differences and root mean square differences of the sea ice extent between the observation and model. The positive and negative signs indicate Cases 1–4 producing larger and smaller error than the "simulation," respectively.

The model results also showed that the influences of the parameterization in Exp#2 were relatively smaller on the sea ice concentration than the sea ice extent. Similarly to that found in Exp#1, the performance in each case was not the same. Regarding the sea ice concentration, Case 1 helped to reduce the mean absolute difference and RMS error by 0.4% and 0.3% (Table 3). Case 2–3 increased the mean absolute differences by 0.7% and 0.9% and the RMS errors by 0.4% and 0.8%, respectively. Case 4 increased the mean absolute difference by 0.1% and decreased the RMS error by 0.1%. Regarding the sea ice extent, Case 1 increasing C_{wi} by 10% reduced the mean absolute difference by 2.7% and the RMS error by 4.8% (Table 3). In Case 2, decreasing C_{wi} by 10% increased the mean absolute difference by 4.9% and the RMS error by 9.4%. In Case 3, increasing θ by 10° increased the mean absolute difference by 0.9% and the RMS error by 1.9%. In Case 4, decreasing θ by 10° reduced the mean absolute difference by 2.4% and the RMS error by 3.3%.

In addition to the air-ice and water-ice drag coefficients and turning angles, the sea ice drift velocity could also be affected by the variability of the oceanic surface current. When the ocean is not fully covered by sea ice, the ocean currents beneath the ice could be influenced by the wind stress on the air-water interface in the ice-free region. We also conducted an additional experiment to examine the influence of the parameterization used for wind stress in the ice-free region on the sea ice drift velocity in the Arctic Ocean. The parameterization methods used in version 4.0 of the Coupled Ocean–Atmosphere Response Experiment (COARE 4.0) have shown a significant improvement in the estimation of the wind stress, particularly during storms [*Edson et al.*, 2013], and are highly recommended for ocean modeling. The comparison between air-water drag coefficients derived by COARE 4.0 and used in our 37 year simulation was made in Figure 17, which showed that the COARE 4.0-derived coefficient is smaller in the weak wind speed range of $<\sim$8 m/s but significantly larger in the wind speed range of $>\sim$10 m/s. Replacing the air-water drag coefficient by the COARE 4.0-derived values, we reran the AO-FVCOM simulation for year 2007. The results did show some improvement in the sea ice drift velocity simulation with error reduction of $\sim$0.7% in the ice drift speed and $\sim$0.2° in the ice drift direction, respectively. In this case, the model result did not show a significant influence on the sea ice concentration and extent. The influence was in the range of $\sim$5.0% or less on the sea ice extent and of $\sim$0.6% or less on the sea ice concentration. These changes, however, are too small to be significant. Since this paper is focused on the ice simulation, no effort was made to evaluate the COARE 4.0 parameterization for the ocean current simulation.

Chen et al. [2016] examined the influences of grid resolution on the multiscale circulation over the continental shelf of the Arctic Basin and transports through Bering Strait, Fram Strait, and the Canadian Arctic Archipelago. The key finding from their studies was that in order to resolve the slope-intensified cyclonic circulation in the Arctic Basin, the horizontal resolution of the model should be consistent with topographic scale and baroclinic internal Rossby deformation radius scale. The AO-FVCOM used for the long-term simulation over the period 1978–2014 was configured with horizontal resolution based on the criterion described in *Chen et al.* [2016]. Extending *Chen et al.* [2016]'s discussion to the sea ice, we compared the ice drift flux through the Barents Sea, Fram Strait, and Bering Strait for the model runs with a horizontal resolution of $\sim$2 km (high-resolution) and $\sim$10 km (coarse resolution). The coarse-resolution model results were obtained from our previous model experiments, which only covered the time period of 1978–2010. For this reason, the comparison was made only over the period 1978–2010. No significant difference was found in the ice drift flux through the sections of the Barents Sea and Fram Strait between the high-resolution and

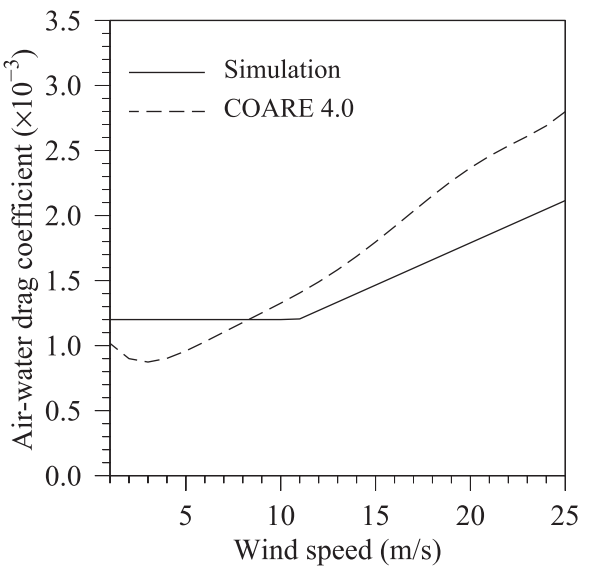

Figure 17. The relationship of the wind drag coefficient on the surface water with wind speed. Black solid line: the drag coefficient used in the AO-FVCOM simulation. Black-dashed line: the drag coefficient parameterized in COARE4.

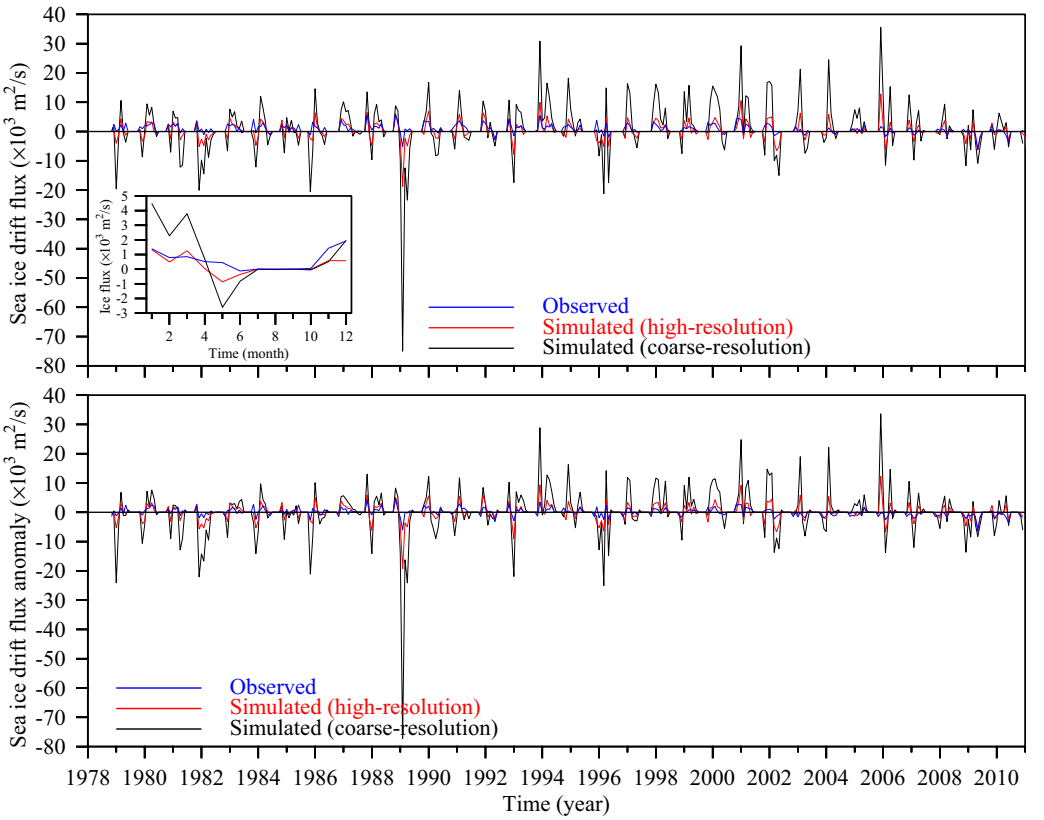

Figure 18. (top) The comparison of the simulated and observed sea ice drift fluxes and (bottom) their anomalies through Bering Strait over the period 1978–2010. (red) The simulated flux obtained from the high-resolution model run; (black) the simulated flux obtained from the coarse-resolution model run; and (blue) the observed flux. The figure inserted in the top plot shows the seasonal variability of the sea ice drift flux per unit ice thickness obtained from observations, high-resolution and coarse-resolution model runs.

coarse-resolution cases, although the high-resolution results slightly showed better results. The model-data correlation was 0.83 for the coarse-resolution case, while it was up to 0.85 for the high-resolution case: only ∼2.0% improvement.

However, increasing the model resolution in Bering Strait and surrounding regions significantly improved the accuracy of the model-simulated ice drift flux through the strait. The model-data discrepancy in the ice drift flux through Bering Strait was 3.69×10^3 m^2/s in the mean absolute difference and 7.18×10^3 m^2/s in the RMS error in the coarse-resolution case. These errors were dropped to 1.08×10^3 m^2/s in the mean absolute difference and 2.02×10^3 m^2/s in the RMS error: 70.7% and 71.9% error reductions in the mean absolute difference and RMS error (Figure 18, top plot). The model-data correlation was 0.59 in the coarse-resolution case, and it was up to 0.64 in the high-resolution case with a critical value of 0.10 at a 95% significance level. The ice drift flux anomaly showed the similar results that the coarse-resolution simulation had a correlation of 0.61 with the observed results and the high-resolution simulation increased the correlation to 0.67 (Figure 18, bottom plot).

It should be pointed here that the model generally produced a larger ice drift flux than the observation, This discrepancy was related to wind stress and not directly related to the horizontal resolution of the model.

6. Summary

The fully ice-sea coupled AO-FVCOM was used to simulate the sea ice in the Arctic Ocean over the period 1978–2014. The model was configured with the unstructured grid with a horizontal resolution of up to ∼2 km. The varying grid resolution was designed to better resolve topographic and baroclinic dynamic

scales over the Arctic slope and in narrow straits and water passages in the CAA. The simulation was conducted with the time and spatial varying boundary conditions provided through a one-way nesting to Global-FVCOM. The model-simulated results for the sea ice were evaluated through comparisons with available sea ice extent, concentration, drift velocity, and thickness.

Without using sea ice data assimilation, the high-resolution AO-FVCOM-simulated sea ice was in good agreement with available observed sea ice extent and reasonable but not as good agreement with concentration, drift velocity, and thickness. This model was capable of resolving not only seasonal and interannual variability of sea ice but also the spatial distribution in the Arctic Ocean. Following the intermodel comparison made by *Johnson et al.* [2012], we carried out the comparison of the AO-FVCOM with six other Arctic Ocean models (ECCO2, GSFC, INMOM, ORCA, NAME, and UW) based on four types of sea ice thickness measurement data. Statistics summarized on Taylor diagrams showed that the AO-FVCOM-simulated ice thickness exhibited a higher correlation coefficient and a smaller residual with observations. The model-produced errors in ice drift speed and direction varied with wind speed. In general, the speed and direction errors enlarged and reduced as the wind speed increased, respectively.

Efforts were also made to examine the sensitivities of the model-produced bias in the ice drift velocity to the parameterization of air-ice external stress and ice-water interfacial stress. The simulation results with different parameterizations of air-ice drag coefficient and turning angle indicates that the ice drift direction was more sensitive to the air-ice drag coefficients and turning angles than the ice drift speed. The parameters used for the 37 year simulation were reasonable, although either a constant air-ice drag coefficient of 1.3×10^{-3} or a fixed turning angle of 20° could slightly reduce the error in the ice drift speed or direction. The experiments with the change of water-ice drag coefficient and turning angles implied that increasing or decreasing either 10% in the drag coefficient or 10° in turning angle did not show a significant influence on the ice drift velocity simulation results, although the sea ice drift speed was more sensitive to these two parameters than the sea ice drift direction. We also examined the impact of different parameterizations of the air-water drag coefficient of wind stress in the sea ice simulation, and no significant influences were found with the use of COARE 4.0 parameterization. Changing the air-ice, ice-water and air-water drag coefficients as well as turning angles had only a slight influence on the sea ice distribution including sea ice concentration and extent.

The simulated accuracy of the sea ice is also relevant to the model grid resolution. Increasing the model resolution in the Bering Strait and surrounding regions significantly improved the accuracy of the model-simulated ice drift flux through the strait.

Acknowledgments

This work was supported by NSF grants OCE-1203393 for the UMASSD team and PLR-1203643 for R. C. Beardsley. The AO-FVCOM system was developed with infrastructure support by the Sino-US Joint Innovative Center for Polar Ocean Research (SU-JICPOR), and the International Center for Marine Studies (ICMS), Shanghai Ocean University (SHOU). G. Gao was supported by the Global Change Research Program of China (2015CB953900) and the National Natural Science Foundation of China under grant 41276197. We gratefully thank Andrey Proshutinsky (aproshutinsky@whoi.edu) for providing us the observational data of sea ice thickness used for our comparison and valuable suggestions to improve the assessment of model skill and performance via comparisons with observations. We also want to thank Mark Johnson (majohnson@alaska.edu) for providing the results of the six models used in their analysis in *Johnson et al*. [2012]. We acknowledge here the use of the observational data set of sea ice extent (ftp://sidads.colorado.edu/DATASETS/NOAA/G02135/) and sea ice drift velocity (http://nsidc.org/data/NSIDC-0116) collected by NSIDC. The Bootstrap sea ice concentration data set is from http://nsidc.org/data/NSIDC-0079. The 37 year simulation was conducted on the SU-JICPOR super performance Linux cluster in the ICMS/SHOU and we thank our SHOU collaborators for their efforts on maintenance of the cluster for this research.

References

Blumberg, A. F., and G. L. Mellor (1987), A description of a three-dimensional coastal ocean circulation model, in *Three-Dimensional Coastal Ocean Models, Coastal and Estuarine Sciences*, vol.4, edited by N. Heaps, pp. 1–16, AGU, Washington D. C.

Chen, C., H. Liu, and R. C. Beardsley (2003), An unstructured, finite-volume, three-dimensional, primitive equation ocean model: Application to coastal ocean and estuaries, *J. Atmos. Oceanic Technol.*, *20*, 159–186.

Chen, C., R. C. Beardsley, and G. Cowles (2006), An unstructured grid, finite-volume coastal ocean model (FVCOM) system, *Oceanography*, *19*, 78–89.

Chen, C., G. Gao, J. Qi, A. Proshutinsky, R. C. Beardsley, Z. Kowalik, H. Lin, and G. Cowles (2009), A new high-resolution unstructured grid finite volume Arctic Ocean model (AO-FVCOM): An application for tidal studies, *J. Geophys. Res.*, *114*, C08017, doi:10.1029/2008JC004941.

Chen, C., et al. (2013), An Unstructured-Grid, Finite-Volume Community Ocean Model FVCOM User Manual, 3rd ed., *Tech. Rep. SMAST/UMASSD-13-0701*, 404 pp., Univ. of Mass, Dartmouth, New Bedford.

Chen, C., G. Gao, Y. Zhang, R. C. Beardsley, Z. Lai, J. Qi and H. Lin (2016), Circulation in the Arcric Ocen: Results from a high-resolution coupled ice-sea nested Global-FVOM and Arctic-FVCOM system, *Prog. Oceanogr.*, *141*, 60–80, doi:10.1016/j.pocean.2015.12.002.

Comiso, J. (2000), *Bootstrap Sea Ice Concentrations from Nimbus-7 SMMR and DMSP SSM/I-SSM/S*, digital media, Natl. Snow and Ice Data Cent., Boulder, Colo.

Comiso, J. (2006), Arctic warming signals from satellite observations, *Weather*, *61*(3), 70–76.

Comiso, J. C. (2012), Large decadal decline of the Arctic multiyear ice cover, *J. Clim.*, *25*(4), 1176–1193.

Edson, J. B., et al. (2013), On the exchange of momentum over the open ocean, *J. Phys. Oceanogr.*, *43*(8), 1589–1610.

Feltham, D. L., M. G. Worster, and J. Wettlaufer (2002), The influence of ocean flow on newly forming sea ice, *J. Geophys. Res.*, *107*(C2), 3009, doi:10.1029/2000JC000559.

Fetterer, F., K. Knowles, W. Meier, and M. Savoie (2002), *Sea Ice Index*, digital media, Natl. Snow and Ice Data Cent., Boulder, Colo.

Flato, G., and G. Boer (2001), Warming asymmetry in climate change simulations, *Geophys. Res. Lett.*, *28*(1), 195–198.

Gao, G., C. Chen, J. Qi, and R. C. Beardsley (2011), An unstructured-grid, finite-volume sea ice model: Development, validation, and application, *J. Geophys. Res.*, *116*, C00D04, doi:10.1029/2010JC006688.

Haas, C., J. Lobach, S. Hendricks, L. Rabenstein, and A. Pfaffling (2009), Helicopter-borne measurements of sea ice thickness, using a small and lightweight, digital EM system, *J. Appl. Geophys.*, *67*(3), 234–241.

Haas, C., S. Gerland, H. Eicken, and H. Miller (1997), Comparison of sea-ice thickness measurements under summer and winter conditions in the Arctic using a small electromagnetic induction device, *Geophysics*, *62*(3), 749–757.
Hall, A. (2004), The role of surface albedo feedback in climate, *J. Clim.*, *17*(7), 1550–1568.
Hibler, W. (1979), A dynamic thermodynamic sea ice model, *J. Phys. Oceanogr.*, *9*(4), 815–846.
Hunke, E. C. (2001), Viscous–plastic sea ice dynamics with the EVP model: Linearization issues, *J. Comput. Phys.*, *170*(1), 18–38.
Hunke, E. C., and J. Dukowicz (1997), An elastic-viscous-plastic model for sea ice dynamics, *J. Phys. Oceanogr.*, *27*(9), 1849–1867.
Hunke, E. C., W. H. Lipscomb, and A. K. Turner (2010), CICE: *The Los Alamos Sea Ice Model Documentation and Software User's Manual, version 4.1, Tech. Rep. LA-CC-06-012*, Los Alamos Natl. Lab., Los Alamos, N. M.
Johnson, M., S. Gaffigan, E. Hunke, and R. Gerdes (2007), A comparison of Arctic Ocean sea ice concentration among the coordinated AOMIP model experiments, *J. Geophys. Res.*, *112*, C04S11, doi:10.1029/2006JC003690.
Johnson, M., A. Proshutinsky, Y. Aksenov, A. T. Nguyen, R. Lindsay, C. Haas, J. Zhang, N. Diansky, R. Kwok, and W. Maslowski (2012), Evaluation of Arctic sea ice thickness simulated by Arctic Ocean Model Intercomparison Project models, *J. Geophys. Res.*, *117*, C00D13, doi:10.1029/2011JC007257.
Kalnay, E., M. Kanamitsu, R. Kistler, W. Collins, D. Deaven, L. Gandin, M. Iredell, S. Saha, G. White, and J. Woollen (1996), The NCEP/NCAR 40-year reanalysis project, *Bull. Am. Meteorol. Soc.*, *77*(3), 437–471.
Kwok, R., and D. Rothrock (2009), Decline in Arctic sea ice thickness from submarine and ICESat records: 1958–2008, *Geophys. Res. Lett.*, *36*, L15501, doi:10.1029/2009GL039035.
Kwok, R., G. Cunningham, M. Wensnahan, I. Rigor, H. Zwally, and D. Yi (2009), Thinning and volume loss of the Arctic Ocean sea ice cover: 2003–2008, *J. Geophys. Res.*, *114*, C07005, doi:10.1029/2009JC005312.
Large, W., and S. Yeager (2009), The global climatology of an interannually varying air–sea flux data set, *Clim. Dyn.*, *33*(2–3), 341–364.
Lipscomb, W. H., E. C. Hunke, W. Maslowski, and J. Jakacki (2007), Ridging, strength, and stability in high-resolution sea ice models, *J. Geophys. Res.*, *112*, C03S91, doi:10.1029/2005JC003355.
Losch, M., D. Menemenlis, J.-M. Campin, P. Heimbach, and C. Hill (2010), On the formulation of sea-ice models. Part 1: Effects of different solver implementations and parameterizations, *Ocean Modell.*, *33*(1), 129–144.
Lytle, V., and S. Ackley (1996), Heat flux through sea ice in the western Weddell Sea: Convective and conductive transfer processes, *J. Geophys. Res.*, *101*(C4), 8853–8868.
Madec, G. (2008), NEMO reference manual, ocean dynamic component: NEMO-OPA, version 3.6, Tech. Rep. 27, *Note du pôle de modélisation*, Inst. Pierre Simmon Laplace (IPSL), France.
Marshall, J., A. Adcroft, C. Hill, L. Perelman, and C. Heisey (1997), A finite-volume, incompressible Navier Stokes model for studies of the ocean on parallel computers, *J. Geophys. Res.*, *102*(C3), 5753–5766.
Mårtensson, S., H. Meier, P. Pemberton, and J. Haapala (2012), Ridged sea ice characteristics in the Arctic from a coupled multicategory sea ice model, *J. Geophys. Res.*, *117*, C00D15, doi:10.1029/2010JC006936.
Martin, T., M. Steele, and J. Zhang (2014), Seasonality and long-term trend of Arctic Ocean surface stress in a model, *J. Geophys. Res. Oceans*, *119*, 1723–1738, doi:10.1002/2013JC009425.
Martin, T., M. Tsamados, D. Schroeder, and D. L. Feltham (2016), The impact of variable sea ice roughness on changes in Arctic Ocean surface stress: A model study, *J. Geophys. Res. Oceans*, *121*, 1931–1952, doi:10.1002/2015JC011186.
Maslowski, W., D. Marble, W. Walczowski, U. Schauer, J. L. Clement, and A. J. Semtner (2004), On climatological mass, heat, and salt transports through the Barents Sea and Fram Strait from a pan-Arctic coupled ice-ocean model simulation, *J. Geophys. Res.*, *109*, C03032, doi:10.1029/2001JC001039.
Maykut, G., and M. G. McPhee (1995), Solar heating of the Arctic mixed layer, *J. Geophys. Res.*, *100*(C12), 24,691–24,703.
Mellor, G. L., M. G. McPhee, and M. Steele (1986), Ice-seawater turbulent boundary layer interaction with melting or freezing, *J. Phys. Oceanogr.*, *16*(11), 1829–1846.
Mellor, G. L., S. M. Häkkinen, T. Ezer, and R. C. Patchen (2002), A generalization of a sigma coordinate ocean model and an intercomparison of model vertical grids, in *Ocean Forecasting*, edited by N. Pinardi and J. D. Woods, pp. 55–72, Springer, New York.
Nguyen, A. T., D. Menemenlis, and R. Kwok (2011), Arctic ice-ocean simulation with optimized model parameters: Approach and assessment, *J. Geophys. Res.*, *116*, C04025, doi:10.1029/2010JC006573.
Parkinson, C. L., and W. M. Washington (1979), A large-scale numerical model of sea ice, *J. Geophys. Res.*, *84*(C1), 311–337.
Perovich, D. K., B. Light, H. Eicken, K. F. Jones, K. Runciman, and S. V. Nghiem (2007), Increasing solar heating of the Arctic Ocean and adjacent seas, 1979–2005: Attribution and role in the ice-albedo feedback, *Geophys. Res. Lett.*, *34*, L19505, doi:10.1029/2007GL031480.
Preller, R. H. (1999), Prediction in ice-covered shallow seas, *Coastal Estuarine Stud.*, *56*, 405–441.
Proshutinsky, A., and M. Johnson (1997), Two circulation regimes of the wind-driven Arctic Ocean, *J. Geophys. Res.*, *102*(C6), 12,493–12,514.
Romanov, I. P. (1995), *Atlas of Ice and Snow of the Arctic Basin and Siberian Shelf Seas*, 2nd ed., translated from Russian by A. Tunik, Backbone, Paramus, N. J.
Rosati, A., and K. Miyakoda (1988), A general circulation model for upper ocean simulation, *J. Phys. Oceanogr.*, *18*(11), 1601–1626.
Rothrock, D. (1975), The energetics of the plastic deformation of pack ice by ridging, *J. Geophys. Res.*, *80*(33), 4514–4519.
Rothrock, D., Y. Yu, and G. A. Maykut (1999), Thinning of the Arctic sea-ice cover, *Geophys. Res. Lett.*, *26*(23), 3469–3472.
Rothrock, D., D. Percival, and M. Wensnahan (2008), The decline in arctic sea-ice thickness: Separating the spatial, annual, and interannual variability in a quarter century of submarine data, *J. Geophys. Res.*, *113*, C05003, doi:10.1029/2007JC004252.
Screen, J. A., and I. Simmonds (2010), The central role of diminishing sea ice in recent Arctic temperature amplification, *Nature*, *464*(7293), 1334–1337.
Serreze, M. C., M. M. Holland, and J. Stroeve (2007), Perspectives on the Arctic's shrinking sea-ice cover, *Science*, *315*(5818), 1533–1536.
Smith, R., J. Dukowicz, and R. Malone (1992), Parallel ocean general circulation modeling, *Physica D*, *60*(1), 38–61.
Sturm, M., D. K. Perovich, and J. Holmgren (2002), Thermal conductivity and heat transfer through the snow on the ice of the Beaufort Sea, *J. Geophys. Res.*, *107*(C21), 8043, doi:10.1029/2000JC000409.
Taylor, K. E. (2001), Summarizing multiple aspects of model performance in a single diagram, *J. Geophys. Res.*, *106*(D7), 7183–7192.
Terwisscha van Scheltinga, A. D. T., P. G. Myers, and J. D. Pietrzak (2010), A finite element sea ice model of the Canadian Arctic Archipelago, *Ocean Dyn.*, *60*(6), 1539–1558.
Thorndike, A., D. Rothrock, G. Maykut, and R. Colony (1975), The thickness distribution of sea ice, *J. Geophys. Res.*, *80*(33), 4501–4513.
Tian, R., C. Chen, J. Qi, R. Ji, R. C. Beardsley, and C. Davis (2015), Model study of nutrient and phytoplankton dynamics in the Gulf of Maine: Patterns and drivers for seasonal and interannual variability, *ICES J. Mar. Sci.*, *72*(2), 388–402, doi:10.1093/icesjms/fsu090.
Tschudi, M., C. Fowler, J. Maslanik, J. S. Stewart, and W. Meier (2016), *Polar Pathfinder Daily 25 km EASE-Grid Sea Ice Motion Vectors, Version 3*, digital media, Natl. Snow and Ice Data Cent., Boulder, Colo.

Volodin, E., N. Dianskii, and A. Gusev (2010), Simulating present-day climate with the INMCM4.0 coupled model of the atmospheric and oceanic general circulations, *Izv. Atmos. Oceanic Phys.*, *46*(4), 414–431.

Zhang, J., and D. Rothrock (2003), Modeling global sea ice with a thickness and enthalpy distribution model in generalized curvilinear coordinates, *Mon. Weather Rev.*, *131*(5), 845–861.

Zhang, Y., C. Chen, R. C. Beardsley, G. Gao, Z. Lai, B. Curry, C. M. Lee, H. Lin, J. Qi, and Q. Xu (2016), Studies of the Canadian Arctic Archipelago water transport and its relationship to basin-local forcings: Results from AO-FVCOM, *J. Geophys. Res. Oceans*, *121*, 4392–4415, doi: 10.1002/2016JC011634.